Global Biogeochemical Cycles®

RESEARCH ARTICLE
10.1029/2023GB007969

Permafrost Region Greenhouse Gas Budgets Suggest a Weak CO_2 Sink and CH_4 and N_2O Sources, But Magnitudes Differ Between Top-Down and Bottom-Up Methods

G. Hugelius[1], J. Ramage[1], E. Burke[2], A. Chatterjee[3], T. L. Smallman[4], T. Aalto[5], A. Bastos[6], C. Biasi[7,8], J. G. Canadell[9], N. Chandra[10], F. Chevallier[11], P. Ciais[11], J. Chang[12], L. Feng[13], M. W. Jones[14], T. Kleinen[15], M. Kuhn[16], R. Lauerwald[17], J. Liu[3], E. López-Blanco[18,19], I. T. Luijkx[20], M. E. Marushchak[21], S. M. Natali[22], Y. Niwa[23,24], D. Olefeldt[25], P. I. Palmer[13], P. K. Patra[26], W. Peters[20,27], S. Potter[22], B. Poulter[28], B. M. Rogers[22], W. J. Riley[29], M. Saunois[11], E. A. G. Schuur[30], R. L. Thompson[31], C. Treat[32], A. Tsuruta[5], M. R. Turetsky[33], A.-M. Virkkala[22], C. Voigt[21,34], J. Watts[22], Q. Zhu[29], and B. Zheng[35]

[1]Department of Physical Geography and Bolin Centre for Climate Research, Stockholm University, Stockholm, Sweden, [2]Met Office Hadley Centre, Exeter, UK, [3]Jet Propulsion Laboratory, California Institute of Technology, Pasadena, CA, USA, [4]School of GeoSciences and National Centre for Earth Observation, University of Edinburgh, Edinburgh, UK, [5]Finnish Meteorological Institute, Helsinki, Finland, [6]Department of Biogeochemical Integration, Max Planck Institute for Biogeochemistry, Jena, Germany, [7]Department of Environmental and Biological Sciences, University of Eastern Finland, Kuopio, Finland, [8]Department of Ecology, Finland and University of Innsbruck, Innsbruck, Austria, [9]Global Carbon Project, CSIRO Environment, Canberra, ACT, Australia, [10]Research Institute for Global Change, JAMSTEC, Yokohama, Japan, [11]Laboratoire des Sciences du Climat et de l'Environnement, LSCE-IPSL (CEA-CNRS-UVSQ), Université Paris-Saclay 91191 Gif-sur-Yvette, Gif-sur-Yvette, France, [12]College of Environmental and Resource Sciences, Zhejiang University, Hangzhou, China, [13]National Center for Earth Observation, University of Edinburgh, Edinburgh, UK, [14]Tyndall Centre for Climate Change Research, School of Environmental Sciences, University of East Anglia (UEA), Norwich, UK, [15]Max Planck Institute for Meteorology, Hamburg, Germany, [16]Department of Earth Sciences, University of New Hampshire, Durham, NH, USA, [17]Université Paris-Saclay, INRAE, AgroParisTech, UMR Ecosys, Palaiseau, France, [18]Department of Ecoscience, Arctic Research Center, Aarhus University, Aarhus, Denmark, [19]Department of Environment and Minerals, Greenland Institute of Natural Resources, Nuuk, Greenland, [20]Meteorology and Air Quality Group, Wageningen University, Wageningen, The Netherlands, [21]Department of Environmental and Biological Sciences, University of Eastern Finland, Kuopio, Finland, [22]Woodwell Climate Research Center, Falmouth, MA, USA, [23]Earth System Division, National Institute for Environmental Studies, Tsukuba, Japan, [24]Department of Climate and Geochemistry Research, Meteorological Research Institute, Tsukuba, Japan, [25]Department of Renewable Resources, University of Alberta, Edmonton, AB, Canada, [26]Research Institute for Humanity and Research, Kyoto, Japan, [27]University of Groningen, Centre for Isotope Research, AG Groningen, The Netherlands, [28]NASA GSFC, Biospheric Sciences Lab, Greenbelt, MD, USA, [29]Climate and Ecosystem Sciences Division, Lawrence Berkeley National Laboratory, Berkeley, CA, USA, [30]Department of Biological Sciences, Center for Ecosystem Science and Society, Northern Arizona University, Flagstaff, AZ, USA, [31]NILU, Kjeller, Norway, [32]Alfred Wegener Institute Helmholtz Center for Polar and Marine Research, Potsdam, Germany, [33]Institute of Arctic and Alpine Research and Department of Ecology and Evolutionary Biology, University of Colorado, Boulder, CO, USA, [34]Institute of Soil Science, University of Hamburg, Hamburg, Germany, [35]Shenzhen Key Laboratory of Ecological Remediation and Carbon Sequestration, Institute of Environment and Ecology, Tsinghua Shenzhen International Graduate School, Tsinghua University, Shenzhen, China

Key Points:

- The northern terrestrial permafrost region was a weak annual CO_2 sink and stable source of CH_4 and N_2O during the time period 2000–2020
- The global warming potential is indistinguishable from neutral over a 100 years time period but a net source of warming over a 20 year period
- Bottom-up and top-down methods yield different magnitudes of estimates that cannot be fully reconciled

Supporting Information:

Supporting Information may be found in the online version of this article.

Correspondence to:

G. Hugelius,
gustaf.hugelius@natgeo.su.se

Citation:

Hugelius, G., Ramage, J., Burke, E., Chatterjee, A., Smallman, T. L., Aalto, T., et al. (2024). Permafrost region greenhouse gas budgets suggest a weak CO_2 sink and CH_4 and N_2O sources, but magnitudes differ between top-down and bottom-up methods. *Global Biogeochemical Cycles*, *38*, e2023GB007969. https://doi.org/10.1029/2023GB007969

Received 8 SEP 2023
Accepted 16 AUG 2024

Abstract Large stocks of soil carbon (C) and nitrogen (N) in northern permafrost soils are vulnerable to remobilization under climate change. However, there are large uncertainties in present-day greenhouse gas (GHG) budgets. We compare bottom-up (data-driven upscaling and process-based models) and top-down (atmospheric inversion models) budgets of carbon dioxide (CO_2), methane (CH_4) and nitrous oxide (N_2O) as well as lateral fluxes of C and N across the region over 2000–2020. Bottom-up approaches estimate higher land-to-atmosphere fluxes for all GHGs. Both bottom-up and top-down approaches show a sink of CO_2 in natural ecosystems (bottom-up: −29 (−709, 455), top-down: −587 (−862, −312) Tg CO_2-C yr^{-1}) and sources of CH_4 (bottom-up: 38 (22, 53), top-down: 15 (11, 18) Tg CH_4-C yr^{-1}) and N_2O (bottom-up: 0.7 (0.1, 1.3), top-down: 0.09 (−0.19, 0.37) Tg N_2O-N yr^{-1}). The combined global warming potential of all three gases (GWP-100) cannot be distinguished from neutral. Over shorter timescales (GWP-20), the region is a net GHG source because CH_4 dominates the total forcing. The net CO_2 sink in Boreal forests and wetlands is largely offset by fires and inland water CO_2 emissions as well as CH_4 emissions from wetlands and inland waters,

with a smaller contribution from N_2O emissions. Priorities for future research include the representation of inland waters in process-based models and the compilation of process-model ensembles for CH_4 and N_2O. Discrepancies between bottom-up and top-down methods call for analyses of how prior flux ensembles impact inversion budgets, more and well-distributed in situ GHG measurements and improved resolution in upscaling techniques.

Plain Language Summary The northern permafrost region covers large areas and stores very large amounts of carbon and nitrogen in soils and sediments. With climate change, there is concern that thawing permafrost will release greenhouse gases into the atmosphere, shifting the region from long-term cooling of the global climate to a net warming effect. In this study, we used different techniques to assess the greenhouse gas budgets of carbon dioxide, methane and nitrous oxide for the time period 2000–2020. We find that the region is a net sink of carbon dioxide, mainly in boreal forests and wetlands, while carbon dioxide is emitted from inland waters and fires affecting both forest and tundra. Lakes and wetlands are strong sources of methane, which contributes to warm the climate significantly, especially over shorter timescales. Nitrous oxide is emitted at low rates across the region, with a relatively limited impact on climate. In summary, the climate warming from the northern permafrost region is likely close to neutral when calculated over a 100 years time window, but it warms the climate when calculated over a 20 years time window.

1. Introduction

The northern terrestrial permafrost region is dominated by taiga and tundra ecosystems, and is an important component in the global cycles of carbon (C) and nitrogen (N) (Obu et al., 2019; Schuur et al., 2022). The permafrost region is warming at rates 2–4 times faster than the global average, causing permafrost thaw (Biskaborn et al., 2019; Rantanen et al., 2022). Warming of the active layer and permafrost, as well as gradual and abrupt thaw, occur across the permafrost domain (Nitze et al., 2018; Runge et al., 2022; Smith et al., 2022) and may increase decomposition of soil organic matter (SOM), rich in both C and N, which has accumulated over millennia under cold and wet conditions. Permafrost region soils are estimated to store 1,000 ± 200 Pg of organic C and 60 ± 20 Pg of N in the upper 3 m (Hugelius et al., 2014; Mishra et al., 2021; Palmtag et al., 2022). Of the total C storage, about 330 ± 80 Pg C is stored in peatlands (Hugelius et al., 2014, 2020) and the rest in mineral soil. In addition to peart formation, soil carbon stocks are often enriched by repeated deposition or frost heave processes (Tarnocai et al., 2009). Additional unconsolidated sedimentary deposits below 3 m depth store an estimated 400–1,000 Pg C, making the permafrost region the largest terrestrial C and N pool on Earth (Strauss et al., 2021). Climate change and permafrost thaw interact with other ecosystem properties, including vegetation, disturbance regimes, and the distribution and flow of water through the landscape (Treharne et al., 2022). All of these factors affect the seasonal and annual budgets of the main greenhouse gases (GHGs) carbon dioxide (CO_2), methane (CH_4), and nitrous oxide (N_2O) as well as aquatic fluxes of C and N.

As soils thaw or become warmer, enhanced microbial processing of soil C and N causes release of GHGs into the atmosphere, causing further warming. This feedback loop is known as the "permafrost carbon feedback" (Schuur et al., 2008, 2022) that can be expanded to "permafrost GHG feedback" by including non-carbon feedbacks, such as from N_2O. The sixth assessment report of the Intergovernmental Panel on Climate Change (IPCC) (Canadell et al., 2021) estimated that the permafrost GHG feedback from CO_2 per degree of global warming at the end of the century is 18 (3.1%–41%, 5%–95% range) Pg C $°C^{-1}$, with an additional permafrost GHG feedback from CH_4 of 2.8 (0.7–7.3) Pg Ceq $°C^{-1}$. However, this IPCC estimate does not fully include abrupt permafrost thaw processes which cause additional release of CO_2 and CH_4 at decadal to centennial time scales, especially from release of CH_4 from water-logged post-thaw environments (Turetsky et al., 2020). Abrupt thaw, including thaw-lake formation, collapse of permafrost peatlands, and thaw-slump formation, can rapidly affect permafrost at depths of several meters, causing rapid melting of ground ice, land subsidence, and complete restructuring of the landscape.

In addition to uncertainties in how climate warming drives increased soil respiration, there is large uncertainty regarding mediating effects from increased vegetation productivity (and CO_2 uptake) caused by longer growing seasons, increased atmospheric CO_2 concentrations, and additional nutrient release from thawing permafrost

(Abbott et al., 2016; Liu, Kimball, et al., 2022; Liu, Kuhn, et al., 2022; McGuire et al., 2018). While uncertainties remain large, many studies based on observational GHG flux time series show enhanced net GHG emissions from warming and thawing permafrost soils (Kuhn et al., 2021; Marushchak et al., 2021; Natali et al., 2015; Rodenhizer et al., 2022; Voigt et al., 2017, 2019).

A potential shift from a net GHG sink to a source remains uncertain in projections using Earth System models (ESMs). A recent study using the sixth phase of the Coupled Model Intercomparison Project (CMIP6) ensemble of ESMs projects a sustained northern CO_2 sink from 2015 to 2100 across a broad range of human emissions scenarios (Qiu et al., 2023). However, the majority of the CMIP6 models do not include an explicit representation of permafrost or GHG feedback from thaw and are thus likely unable to properly project changes in permafrost GHG balance under future warming (Burke et al., 2020; Varney et al., 2022). A previous intercomparison of process-models with representation of gradual permafrost thaw found that the northern permafrost region would act as a sustained net C sink under medium emission scenarios (RCP4.5) but would likely act as a C source under higher emissions scenarios, at least over the 21st century (McGuire et al., 2018). However, there was significant spread between the models, reflecting limited representation of processes affecting vegetation productivity, soil respiration and permafrost dynamics. There is also mounting evidence that other localized disturbance processes, still lacking in global models, play an important role in the mobilization of permafrost C and N. In addition to abrupt thaw, this includes disturbances associated with fires, pests, or windfalls (Foster et al., 2022; Holloway et al., 2020; Walker et al., 2019). While progress is continuously being made, model simulations of the interactions between permafrost and disturbances are in their infancy (Treharne et al., 2022) and are often only relevant for specific field sites (Aas et al., 2019; López-Blanco et al., 2022). Similarly, the lateral export of C and N from land to sea in the form of riverine dissolved organic C or N (DOC, DON) or coastal erosion is missing in most ESMs. Moreover, process information and dedicated simulations for permafrost region N_2O fluxes are still scarce (Voigt et al., 2020).

Improved understanding of GHG exchange in the permafrost region is therefore crucial for constraining global GHG budget estimates and reducing discrepancies between methods (Friedlingstein et al., 2022; Saunois et al., 2020; Tian et al., 2020). Estimates of GHG budgets are typically done using bottom-up (from data-driven ecosystem flux upscaling–hereafter referred to as ecosystem flux upscaling–or process-based models) or top-down (from inversions of atmospheric GHG mole fractions–hereafter referred to as atmospheric inversion models) approaches (Ciais et al., 2022). Budgets based on ecosystem flux upscaling combine observations of GHG fluxes with geospatial data sets, while process-based model budgets are based on mathematical representations of ecosystems, biogeochemical and physical processes. It may also involve model-data fusion (MDF) approaches, where a process-model is calibrated at pixel-scale using spatially coherent observations interpolated from field data and satellite-based Earth Observation (EO) (Bloom et al., 2016). The top-down approach is based on atmospheric inversion models, which use advanced mathematical methods to estimate surface-to-atmosphere net GHG fluxes by combining atmospheric GHG concentration information (in-situ or flask measurements or total column abundances estimated from remote sensing), gridded prior flux information, and atmospheric transport models.

The first comprehensive GHG budget synthesizing bottom-up and top-down GHG estimates for the Arctic tundra was published in 2012 as part of the REgional Carbon Cycle Assessment and Processes project (RECCAP, McGuire et al., 2012) and highlighted the high variability between budgeting methods. While more process-based model estimates include relevant processes (e.g., McGuire et al., 2018), the periodic evaluation of these bottom-up approaches is critical to understanding the current strengths and weaknesses of the different approaches and where the best path for improvement lies.

Here we present comprehensive GHG (CO_2, CH_4, and N_2O) budgets obtained through bottom-up and top-down approaches for the period 2000–2020 across the terrestrial northern permafrost region. The budgets also include estimated anthropogenic emissions of CO_2 and CH_4 as well as lateral fluxes of C and N from rivers and coastal erosion. We then compare these GHG budgets and identify the remaining research gaps that must be addressed in order to reconcile the different budgets and improve their interpretation. These permafrost regional budgets are part of the REgional Carbon Cycle Assessment and Processes-2 (RECCAP2) project of the Global Carbon Project that aims to collect and integrate regional GHGs budgets covering all global lands and oceans (Ciais et al., 2022) (https://www.globalcarbonproject.org/reccap/).

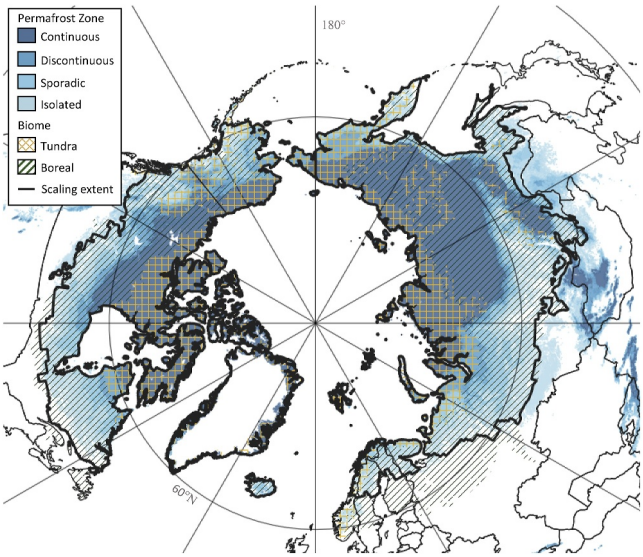

Figure 1. Map of the extent of the study area, defined as the northern permafrost region (blue shades, data from Obu, 2021) overlaps with the spatial extent of the Tundra and Boreal Forest biomes (hatched areas) as represented Boreal Arctic Wetlands and Lakes Data set (BAWLD, Olefeldt et al., 2021). Because the permafrost extent is non-continuous in much of the region, it includes large areas of permafrost-free ecosystems in a mosaic within the broader region. Figure S1 in Supporting Information S1 in the supplement shows the additional areas that recorded mean annual air temperature (MAAT) below 0°C between 1990 and 2000 (full extent of specific permafrost model intercomparisons), but which were excluded from this budget estimate because they are outside the BAWLD extent.

2. Methods

2.1. Study Area

Permafrost is ground that is at or below 0°C for at least two consecutive years and underlies circa 14 million km^2 of land in the Northern Hemisphere (Obu, 2021). The northern permafrost region by definition also includes areas with spatially discontinuous permafrost coverage, and covers circa 22 million km^2 of land when permafrost-free areas within the region are included (Obu, 2021). The spatial extent of this study area includes the terrestrial northern permafrost region as defined in Obu (2021) and its overlap with the Boreal Arctic Wetlands and Lakes Data set area (BAWLD) (Olefeldt et al., 2021) (Figure 1). The BAWLD-RECCAP2 permafrost region considered in this study is 18.42 million km^2 (excluding ice sheets and glaciers). Because much of the region is underlain by spatially discontinuous permafrost in a mosaic of different landforms and ecosystems, areas and land cover types without permafrost are included in the domain. The BAWLD region was selected due to constraints in data availability for ecosystem flux upscaling. The targeted BAWLD-RECCAP2 permafrost domain does not consider areas underlain by permafrost in Central Asia and the Tibetan plateau (blue areas outside the black line in Figure 1). All flux estimates and models were run or rescaled to 0.5° × 0.5° spatial resolution and masked to match the BAWLD-RECCAP2 permafrost region (hereafter permafrost region). We differentiated tundra and boreal forest areas within the permafrost region using a biome delineation (Dinerstein et al., 2017). The study area overlaps several other RECCAP2 regions (Ciais et al., 2022, Figure S1 in Supporting Information S1). Because other regions have used very different methods and/or because work has progressed at different time schedules, no effort has been made to harmonize the budgets between regions made in this paper.

2.2. Summary of Overall Budget Approach

We present the most complete budgets of C and N fluxes for the main GHGs (CO_2, CH_4 and N_2O) for the period 2000–2020 derived from different approaches: process-based models, data-driven ecosystem upscaling, and atmospheric inversion models (Figure 2, Table 1). Budget. also include lateral fluxes of C and N from streams and rivers as well as from coastal erosion. Other GHGs, such as biogenic volatile organic compounds, are not included in these budgets. The budgets are compiled from a large and diverse collection of published and unpublished data sets. Process-based model budgets rely on a set of model ensemble estimates as well as model-data fusion (MDF) with the CARbon DAta MOdel fraMework (CARDAMOM) (Bloom et al., 2016). Data-driven ecosystem upscaling budgets are adapted from Ramage et al. (2024). Top-down budgets are derived from analyses of inversion model ensembles.

All budgets are expressed on a C and N mass basis (i.e., for GHGs as CO_2-C, CH_4-C and N_2O-N yr^{-1}), reported as Tg C or N, and are given as mean fluxes with 95% confidence intervals (CI). Consistent with global GHG budgets (Friedlingstein et al., 2022; Saunois et al., 2020; Tian et al., 2020), sinks into the biosphere are reported as negative numbers, while sources to the atmosphere are reported as positive numbers. To estimate the total combined radiative balance of the permafrost region GHG budgets, all budgets are combined into a common unit of CO_2-C equivalents. This is calculated as Global Warming Potential (GWP) for a 100-year time period (GWP-100 from Table 7.15 in Forster et al., 2021).

2.3. Process-Based Models for Terrestrial CO_2 and Wetland CH_4 Fluxes

2.3.1. Terrestrial CO_2 Fluxes

Estimates of terrestrial ecosystem fluxes of CO_2 were extracted from several model comparisons computed during the last decade. We analyze ensembles of 52 process-based model simulations driven by reanalyzes-based climate data, included in four different model intercomparison projects (summarized in Table S1 in Supporting

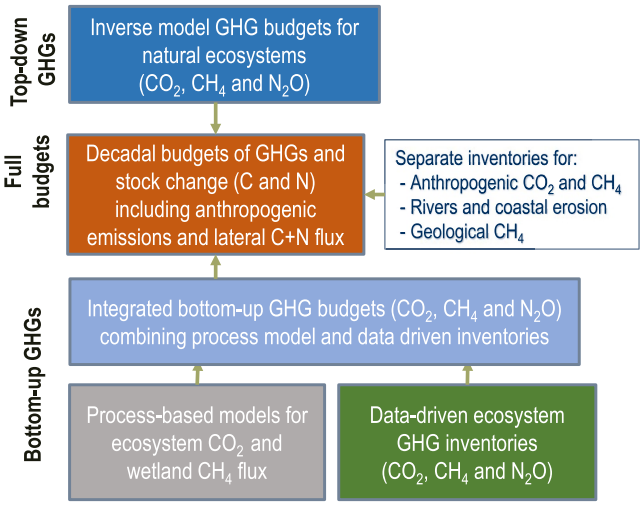

Figure 2. Conceptual figure summarizing the overall approach, including top-down and bottom-up, to compile the RECCAP2 permafrost GHG and lateral flux budgets. The main budget components are presented in blue boxes. The bottom-up process-based models include both ensembles of process-models as well as model-data fusion (MDF) with the CARbon DAta MOdel fraMework (CARDAMOM). Data-driven ecosystem GHG inventories and estimates of lateral fluxes and geological CH_4 are taken from Ramage et al. (2024) Additional budget components in blue text (white box) include separate inventories of anthropogenic fluxes, lateral fluxes (rivers and coastal erosion) and geological emissions which are used to complete the budgets.

Information S1). All models contain their own individual C cycle processes with a range of complexity. Of these 52 simulations, 15 models included layered soils with a representation of permafrost C, which were analyzed as a separate sub-ensemble compared to models without permafrost-specific processes (layered and bulk C, respectively). Wildfire processes are represented in 26 models, and 14 models have both fires and permafrost represented (Table S1 in Supporting Information S1).

2.3.1.1. Model Ensembles and Configurations

We extracted the C stocks and fluxes from both the Permafrost Carbon Network (PCN) and the Multi-scale Synthesis Terrestrial Model Intercomparison Project (MsTMIP) ensembles. These ensembles were extracted via the ORNL DAAC and from the Land Surface, Snow and Soil Moisture Model Intercomparison Project (LS3MIP) land-history simulations driven by observed meteorology via the CMIP6 model archive (Van Den Hurk et al., 2016). Data from the Inter-Sectoral Impact Model Intercomparison Project phase 2a and 2b (ISIMIP2a and ISIMIP2b) were downloaded from https://www.isimip.org. In the case of ISIMIP2a, only the ensemble members driven by the Global Soil Wetness Project version 3 climate forcing (Dirmeyer et al., 2006) data were included. For ISIMIP2b, only the ensemble members driven by bias-corrected climate data from the IPSL-CM5A-LR Earth System model submitted to the CMIP5 archive were considered. Initial results from ISIMIP phase 3a/3b simulations are also shown for the four models. Results from these model simulations were previously unpublished and described in more detail in the paragraph below. Table S1 in Supporting Information S1 provides a summary of the process models used in the study.

The ISIMIP3 modeling output was retrieved from five models:

1. The Joint UK Land Environment Simulator (JULES), which was driven by GSWP3 meteorology bias corrected by the W5E5 data set (Lange, 2019), denoted GSWP3-W5E5 under the ISIMIP3a protocol. JULES is the land surface component of the UK Earth System Model (UKESM–(Sellar et al., 2019). The configuration of JULES presented here includes the representation of C and N cycling (Wiltshire et al., 2021) but not vertically resolved soil carbon.
2. The Organizing Carbon and Hydrology In Dynamic Ecosystems model (ORCHIDEE) was also driven by GSWP3-W5E5 following the ISIMIP3a protocol. The simulations were performed using ORCHIDEE-MICT (Guimberteau et al., 2018), a version of ORCHIDEE with permafrost C representation in a multilayered vertically discretized model, interactions between soil C, soil temperature and hydrology, and a fire module that burns litter and vegetation. The version used in ISIMIP3a is further improved with the representation of grassland management (Chang et al., 2021) and northern peatlands (Qiu et al., 2020).
3. Two versions of the Jena Scheme for Biosphere Atmosphere Coupling were run (JSBACH-wet and JSBACH-dry). They were driven by GFDL-ESM4 historical forcing, following the ISIMIP3b protocol. JSBACH is the land surface component of the Max Planck Institute for Meteorology Earth System Model MPI-ESM version 1.2 (Mauritsen et al., 2019) with a methane cycle according to (Kleinen et al., 2020). The "wet" and "dry" configurations cover plausible ranges of soil parameters leading to wetter and dryer soil conditions (De Vrese et al., 2023).
4. The Energy Exascale Earth System Land Model with an Equilibrium Chemistry Approximation (ELM-ECA) was driven by climate data from GFDL-ESM4 submitted to the CMIP6 archive. GFDL-ESM4 was bias-corrected by the W5E5 data that was also used in ISIMIP3a. This simulation follows the ISIMIP3b protocol. ELM-ECA is a multilayered land model integrated in the Energy Exascale Earth System Model (E3SM) (Zhu et al., 2019). It simulates C, N, phosphorus, water and energy cycles for major terrestrial ecosystems (e.g., forest, shrub, grassland, wetland). ELM-ECA considers multiple nutrient competitions among plants, microbial immobilizers, nitrifiers, denitrifiers, and mineral surfaces to resolve the resource partitioning among different competitors (Riley et al., 2018). The version used in ISIMIP3b has improved the parameterization of wetland inundation and upland plant carbon-nutrient interactions (Zhu et al., 2024).

Table 1
Method Summary Showing the Data Sources and Approaches Used for the Various Budget Components, Including Relevant References

Model ensemble or configuration	Description and data source	Method section	References
Bottom-up, process-based models			
Terrestrial CO_2 fluxes			
PCN MIP	Ensemble of 10 models from Permafrost Carbon Network (PCN) model intercomparison, data available at ORNL DAAC	2.3.1.1	McGuire et al. (2022)
MsTMIP	Ensemble of 14 models from Multi-scale Synthesis and Terrestrial Model Intercomparison Project, data available at ORNL DAAC	2.3.1.1	Huntzinger et al. (2018)
LS3MIP	Ensemble of 9 models from Land Surface, Snow and Soil Moisture Model Intercomparison Project land-history simulations, data available via the CMIP6 model archive	2.3.1.1	Van Den Hurk et al. (2016)
ISIMIP2a/2b	Ensemble of 14 models from Inter-Sectoral Impact Model Intercomparison Project phase 2a and 2b (ISIMIP2a and ISIMIP2b), data available at https://www.isimip.org	2.3.1.1	Dirmeyer et al. (2006), also see https://www.isimip.org/protocol/2a/
ISIMIP3a/3b	Ensemble of 5 models (previously unpublished) from a subset of Inter-Sectoral Impact Model Intercomparison Project phase 3, data available at https://www.isimip.org	2.3.1.1	Dirmeyer et al. (2006), also see https://www.isimip.org/protocol/3/
CARDAMOM	New assessments from model-data fusion (MDF) with the CARbon DAta MOdel fraMework (CARDAMOM). Data available at https://doi.org/10.7488/ds/7505	2.3.1.2	Bloom et al. (2016) and Smallman and Williams (2023)
Wetland CH4 fluxes			
Model configuration	Description and data source	Method section	References
Wetland model ensemble	Ensemble of 13 wetland models constrained by observed wetland extent	2.3.2	Saunois et al. (2020)
Bottom-up, data-driven upscaling and inventories			
Ecosystem GHG fluxes			
Budget component	Description and data source	Method section	References
Terrestrial CO_2, CH_4, and N_2O flux	Thematic upscaling from BAWLD land cover classes based on synthesis of field-based fluxes	2.4	Olefeldt et al. (2021), Virkkala et al. (2022), Kuhn et al. (2021), Voigt et al. (2020), and Ramage et al. (2024)
Lake CO_2 and CH_4	Thematic upscaling from BAWLD inland water classes based on synthesis of field-based fluxes	2.4	Olefeldt et al. (2021) and Ramage et al. (2024)
Lake N_2O	Extracted from global gridded dataset	2.4	Lauerwald et al. (2019) and Ramage et al. (2024)
Rivers CO_2	Diffusive flux calculated from monthly gridded global data, adapted to ice-free season	2.4	Liu, Kuhn, et al. (2022), Liu, Kimball, et al. (2022) and Ramage et al. (2024)
Rivers CH_4	Calculated from monthly estimated diffusive fluxand river areas from BAWLD	2.4	Stanley et al. (2016), Olefeldt et al. (2021), and Ramage et al. (2024)
Fires, CO_2, CH_4 and N_2O flux	Extracted from the Global Fire Emission Database	2.4	van der Werf et al. (2017) and Ramage et al. (2024)
Abrupt permafrost thaw, CO_2 and CH_4	Extracted from inventory-based abrupt thaw model	2.4	Turetsky et al. (2020) and Ramage et al. (2024)
Geological emsissons, CH_4	Extracted from permafrost region estimate for gas seeps along permafrost boundaries and lake beds	2.4	Walter Anthony et al. (2012) and Ramage et al. (2024)

Table 1
Continued

Lateral fluxes			
Budget component	Description and data source	Method section	References
Riverine transport	Estimated dissolved organic C and N representative for all land north of 60° N	2.4	Terhaar et al. (2021) and Ramage et al. (2024)
Coastal erosion	Spatial estimates of coastal erosion rates multiplied by C and N content in coastal soils	2.4	Lantuit et al. (2012) and Ramage et al. (2024)
Anthopogenic emissions			
Budget component	Description and data source	Method section	References
Anthropogenic CO_2	Extracted Fossil fuel combustion (coal, gas and oil), cement production and cement carbonization from the Global Carbon Project gridded dataset	2.6	Jones et al. (2021, 2022)
Anthropogenic CH_4	Extracted the Fossil fuel plus Agriculture and waste components from spatial datasets of the Global Methane Budget	2.6	Saunois et al. (2020)
Top-down, atmospheric inversions			
Budget component	Description and data source	Method section	References
CO_2 model ensemble	Ensemble of 6 inversion model systems used in the Global Carbon Budget, plus an additional model system	2.7	Friedlingstein et al. (2022) and Chandra et al. (2022)
CH_4 model ensemble	Ensemble of 14 inversion model systems, a sub-ensemble of 22 models used in the Global Methane Budget	2.7	Saunois et al. (2020)
N_2O model ensemble	Ensemble of 2 inversion model systems used in the Global Nitrogen Budget	2.7	Tian et al. (2020)
CO_2 fire flux	Extracted form global gridded inversion-based estimate of fire CO_2 emissions	2.7	Zheng et al. (2023)

2.3.1.2. Analyses of Process Model Output

Analyses of model output were separated into two groups, with models including a representation of permafrost C analyzed as a separate sub-ensemble (layered and bulk C, respectively). The multi-annual mean estimate of the carbon stocks and fluxes was defined for the period 1980 to the end of the model simulation (Table S1 in Supporting Information S1). The mean residence time of dead organic matter (MRT_{SHR}) is defined as the sum of C stored in SOM and litter content divided by heterotrophic respiration. All these models estimate the net ecosystem productivity of CO_2 (NEP = NPP–SHR), where NPP is the net primary productivity and SHR is the soil heterotrophic respiration and positive values are a land sink. Some of the process-models used here also consider the additional impact of aboveground C emissions from fire but none estimate belowground C loss from fire. In this case, the net biosphere productivity is defined, which additionally includes the fire emissions (NPP–SHR–fire). This is important because the majority of fire carbon emissions in the circumpolar domain are from belowground sources: roughly 84%–90% in arctic-boreal North America and 57%–74% in Eurasia (Potter et al., 2023; Veraverbeke et al., 2021; Walker et al., 2020). Other disturbances, such as pest or storm damage to forests, are not systematically represented in these model ensembles and can therefore not be considered here. Fluxes from rivers and lakes are also not considered, as are those from abrupt permafrost thaw since these processes are not represented by any available models. Carbon use efficiency (CUE), defined as the ratio of net primary productivity (NPP) to gross primary productivity (GPP) where NPP = GPP–plant respiration (R_a), is an emergent property of the models that quantifies vegetation efficiency at storing C fixed via photosynthesis on annual timescales. In addition, full ecosystem budgets for CH_4 and N_2O fluxes from process-based models were either not available or not provided for the model intercomparisons (but see separate section for process-based model budgets of wetland CH_4 flux).

2.3.1.3. Model-Data Fusion With CARDAMOM

Observation-informed estimates of terrestrial C stocks, fluxes and ecosystem traits (e.g., MRT_{SHR}) within a consistent mass-balanced framework are essential to support the evaluation of the model ensembles described above. To generate these estimates we use CARDAMOM (Bloom et al., 2016), which has been previously used to inform our understanding of Arctic C-cycling (López-Blanco et al., 2019). CARDAMOM is a model-data fusion framework that uses a Bayesian approach within an adaptive-proposal Markov chain Monte Carlo (AP-MCMC) (Haario et al., 2001) to train a process-model of intermediate complexity, DALEC (Bloom & Williams, 2015; Smallman et al., 2021; Smallman & Williams, 2019). CARDAMOM estimates ensembles of parameter sets for each location independently from each other as a function of location specific data-constraints. These location-specific parameter ensembles result in DALEC simulations consistent with the assimilated data sets, their associated uncertainties and ecological and dynamical constraints (for details see Famiglietti et al., 2021). From these parameter ensembles, CARDAMOM can generate pixel-level estimates of terrestrial C-cycling and their associated uncertainty, allowing a more rigorous evaluation of more complicated process-oriented models which have a less direct connection to data (Caen et al., 2022). Specifically, in this analysis, CARDAMOM analyzed terrestrial C-cycling at a monthly time step and $0.5 \times 0.5°$ spatial resolution for 19 years (2001–2019). The meteorological drivers were drawn from the GSWP3-W5E5 data set, while fire was imposed as a function of the MODIS burned area (Giglio et al., 2018) and forest loss was constrained using global forest watch (Hansen et al., 2013). Assimilated information was time series estimates of leaf area index (Copernicus Service Information 2021), woody biomass for 2017 and 2018 (Santoro et al., 2021), and net biome exchange of CO_2 (Koren, 2020). Moreover, the Northern Circumpolar Soil Carbon Database (NCSCD) provided a pixel specific prior for the initial soil carbon stock (Hugelius, Bockheim, et al., 2013; Hugelius, Tarnocai, et al., 2013). Finally, a globally applied prior for the ratio of autotrophic respiration and photosynthesis of 0.46 ± 0.12 was used (Collalti & Prentice, 2019). For a more detailed description of CARDAMOM, DALEC and its drivers and observational constraints see the supplemental text and Figure S2 in Supporting Information S1. The CARDAMOM data set used for the analyses is available from Smallman and Williams (2023).

2.3.2. Estimated Wetland CH_4 Emissions From Process-Based Models

Wetland CH_4 emissions were extracted from global-scale process model ensembles for the wetland component of the terrestrial land surface produced for the Global Methane Budget (Saunois et al., 2020). Wetlands included peatlands (bogs and fens), mineral soil wetlands (swamps and marshes), and seasonal or permanent floodplains. This excludes exposed water surfaces without emergent macrophytes (such as ponds, lakes and rivers) and coastal vegetated ecosystems. In Saunois et al. (2020), 13 land surface models representing CH_4 exchanges were run for the time period 2000–2017 using a common climatic forcing (see Table 2 in Saunois et al., 2020). For the permafrost region budget, only model runs with wetland extent constrained by the Wetland Area Dynamics for Methane Modeling data set (WAD2M) (Zhang et al., 2021) were used (called "diagnostic model runs" in Saunois et al., 2020). The annual modeled CH_4 wetland budgets were extracted for the permafrost region and summarized per decade. Although the spatial extent of wetlands in BAWLD is not exactly the same as in WAD2M, the two data sets are similar. They are based on partly identical source data and the definition of wetlands applied in WAD2M is consistent with definitions in BAWLD. We therefore consider the estimates to be sufficiently similar that they support the comparison of CH_4 budgets from ecosystem upscaling with estimates from process-based models (i.e., differences between the methods themselves are much larger than differences in wetland area). Table S2 in Supporting Information S1 summarizes the process-based models used to estimate CH_4 wetland fluxes.

2.4. Data Driven Ecosystem GHG and Lateral Flux Budgets

All values reported for data-driven ecosystem flux upscaling of GHG budgets and lateral fluxes presented here are from Ramage et al. (2024). We refer to this study for in-depth method descriptions. Briefly, C and N budgets (2000–2020) were calculated by summing GHG uptake and emissions from terrestrial ecosystems, inland waters, and from disturbances (fire and abrupt thaw) as well as lateral fluxes and geological emissions using several synthesis data sets. The land cover classification used for the analysis was adapted from the BAWLD land cover classification (Olefeldt et al., 2021). The original 19 terrestrial land cover classes in BAWLD were aggregated into five classes: *Boreal forest*, *Non-permafrost wetlands*, *Dry tundra*, *Tundra wetlands* and *Permafrost bogs*. The classes *Dry tundra, Tundra wetlands, and Permafrost bogs* are underlain by near surface permafrost, but differ largely based on wetness and organic soil depth. Because of spatially discontinuous permafrost coverage, *Boreal*

Table 2
Summary of Annual Budgets From Process-Based Model Ensembles and the Model Data-Fusion Approach CARDAMOM

		CO_2	2.5% CI	97.5% CI	CH_4	2.5% CI	97.5% CI
	n models	Tg CO_2-C yr^{-1}			Tg CH_4-C yr^{-1}		
Full model ensemble: NPP- SHR–Ffire	**26**	**−350**	−1040	−150	NA		
sub-ensemble (layered C): NPP- SHR–Ffire	14	−290	−630	−120			
Full model ensemble: NPP–SHR	52	−450	−1,370	−110			
sub-ensemble (layered C): NPP–SHR	15	−490	−890	−130			
Model ensemble: Ffire	26	130	20	460			
sub-ensemble (layered C): Ffire	14	170	20	460			
CARDAMOM: NPP- SHR–Ffire		**−870**	−1,780	160	NA		
CARDAMOM: NPP–SHR		−960	−1,880	20			
CARDAMOM: Ffire		60	50	100			
Model ensemble wetland CH4 flux		NA			**12**	8.6	16

Note. For CO_2 the mean from the full ensemble of models that include fire is presented as well as the annual budgets from CARDAMOM. For CH_4 the annual fluxes from wetlands are reported. No process-based model results are available for N_2O. Bold values indicate the net ecosystem CO_2 balance used for annual budgets.

forests include both permafrost and permafrost-free ecosystems. Mean annual areal fluxes of CO_2, CH_4, and N_2O were obtained for each of the five terrestrial land cover classes by modifying three comprehensive GHG flux data set compilations for CO_2 fluxes (Virkkala et al., 2022), CH_4 fluxes (Kuhn et al., 2021) and N_2O fluxes (Voigt et al., 2020) with addition of N_2O flux data for Boreal forest. Total fluxes were calculated by multiplying the areal flux by the emitting areas for each of the land cover type.

Inland water fluxes of CO_2 and CH_4 to the atmosphere were calculated by upscaling mean annual fluxes from lakes and rivers using the estimated surface area of these aquatic classes from the BAWLD classification, with regional adjustment of ice-covered duration and fluxes during ice break-up (see Ramage et al., 2024 for details). To estimate lake fluxes of N_2O from inland waters, gridded global data of annual flux were used (Lauerwald et al., 2019). Estimates of river and stream CO_2 flux were calculated from gridded monthly flux data (Liu, Kimball, et al., 2022; Liu, Kuhn, et al., 2022) using adjusted surface areas. Riverine CH_4 emissions were determined by combining estimated river surface areas in BAWLD with the mean CH_4 diffusive flux reported in the MethDB database (Stanley et al., 2016). To estimate river fluxes of N_2O, gridded global data of annual full landscape flux were used (Maavara et al., 2019).

Monthly fire emissions of CO_2 and CH_4 were extracted for the study region from the Global Fire Emission Database version 4 for the years 2000–2016 (GFED; van der Werf et al., 2017) and its Beta version to cover emissions from fires between 2017 and 2020. The GFED is driven by estimates of burned areas derived from satellite-based remote sensing data at a spatial resolution of 0.25° (Van Der Werf et al., 2017).

Fluxes of CO_2 and CH_4 from abrupt thaw landforms (thermokarst) were extracted from an inventory-based abrupt thaw model (Turetsky et al., 2020). This model simulates three generalized types of abrupt thaw terrain: mineral-rich lowlands, uplands/hillslopes, and organic-rich wetlands. The abrupt thaw model was initialized for a historical assessment period (1900–2000) and was run for the period 2000–2020 to assess CO_2 and CH_4 emissions from active and stabilized abrupt thaw features. To prevent double counting, fluxes from mineral-rich lowlands and organic-rich wetlands were counted as a sub-flux (not added to the total) of terrestrial land cover fluxes.

Estimates of geological emissions of CH_4 (from subsurface fossil hydrocarbon reservoirs) are from a circumpolar permafrost region estimate for gas seeps along permafrost boundaries and lake beds (Walter Anthony et al., 2012). No separate estimates of geological emission for CO_2 or N_2O are available for the permafrost region.

Lateral C and N fluxes from riverine transport of DOC and DON from the terrestrial permafrost region to the ocean are extracted from a global data set (Terhaar et al., 2021) using data representative for all land north of 60°

N. Emissions from coastal erosion are from (Lantuit et al., 2012), and calculated by multiplying spatially resolved estimates of coastal erosion rates by estimates of C and N content in coastal soils.

2.5. Integrated Bottom-Up Budgets

To reconcile the differences between the varying bottom-up approaches, integrated bottom-up GHG budgets were created by combining the results of the ensembles of process-based models and ecosystem upscaling. The data-driven upscaling (Ramage et al., 2024) includes the full targeted range of landscape components and disturbances. However, the process model ensembles do not fully account for fires and permafrost (lacking in some process models), inland waters and abrupt thaw (lacking in all process models). First, we include only model ensemble net ecosystem exchange (NEE = NPP - SHR–F_{fire}, Figure 3) from the 26 process-based models including fire flux (Table S1 in Supporting Information S1). Then, because these 26 process-based models lack representation of inland waters as well as abrupt thaw, the data-driven estimated CO_2 and CH_4 fluxes from inland water as well as abrupt thaw wetlands (Ramage et al., 2024) are added to the model flux estimates for total CO_2 flux and CH_4 wetland flux. To avoid double counting of areas, the original model fluxes are corrected proportional to the areas occupied by inland waters and abrupt thaw wetlands (−8%; 1.38 out of 17.05 Million km^2). As a final step, the integrated bottom-up budgets are calculated as the mean of the process-based models (after accounting for inland water and abrupt thaw wetlands) and data-driven ecosystem upscaling for upland and wetland ecosystems.

2.6. Anthropogenic Emissions

Estimates of anthropogenic emission are extracted from global data sets, consistent with data used in global GHG budgets (Friedlingstein et al., 2022; Saunois et al., 2020), and other RECCAP2 budgets (Ciais et al., 2022). Estimates of anthropogenic CO_2 emissions from fossil fuel combustion (coal, gas and oil estimated separately), cement production, and cement carbonization were extracted from the Global Carbon Project's gridded data set for fossil CO_2 emissions and related O_2 combustion (GCP-GridFED) (M. W. Jones et al., 2021), updated for the 2022 edition of the Global Carbon Budget (GCP-GridFEDv2022.2; Jones et al., 2022). In GCP-GridFED, the emissions of fossil CO_2 relate to the combustion and use of fossil fuels and the production of cement clinkers. These estimates are consistent at the national and annual levels with the emissions inventory compiled by the Global Carbon Project (Andrew & Peters, 2022; Friedlingstein et al., 2022). Emissions are gridded at 1 km resolution based on the Emissions Database for Global Atmospheric Research (EDGAR) data set, version 4.3.2 (Janssens-Maenhout et al., 2019), and distributed across the months of each year using a relationship with heating and cooling degrees (years 1959–2019) and Carbon Monitor to reflect the impact of COVID-19 (year 2020), as described by Jones et al. (2021, 2022).

Estimates of anthropogenic CH_4 emissions were estimated using the Fossil fuel plus Agriculture and waste components produced for the top-down ensemble of global inversion estimates from Saunois et al. (2020) (available for 2000–2017). We refer to Saunois et al. (2020) for more details on how these data sets were derived. Due to a lack of data access, no separate estimates of anthropogenic N_2O fluxes are included in the study. Anthropogenic N_2O fluxes are primarily from agriculture (Tian et al., 2020), which is largely absent in our study region and it is unlikely that there are significant anthropogenic N_2O sources.

2.7. GHG Budgets From Atmospheric Inversions Models

Independent decadal budgets for CO_2, CH_4 and N_2O are derived from ensembles of inverse model flux estimates. Budgets for 2000–2010 are reported for all GHGs. Due to differing data availability during the second decade, the GHG budgets are reported for different time periods: 2010–2020 for CO_2, 2010–2017 for CH_4, and 2010–2019 for N_2O. Inverse systems for estimating GHGs vary in the time scale of the analysis, the spatiotemporal resolution of the inferred fluxes, or the inverse modeling framework used (Gaubert et al., 2019; Peylin et al., 2013), all of which contribute to differences in the inferred flux estimates. To obtain the best estimates of the GHG budget from atmospheric inversion models, a common method is to derive a mean or median flux estimate and the spread among the estimates from an ensemble of different atmospheric inversion models (Ciais et al., 2022; Philip et al., 2022). The inverse model systems used to derive annual GHG budgets in this study are summarized in Table S3 in Supporting Information S1.

The analyses followed the RECCAP2 protocol to estimate CO_2, CH_4 and N_2O fluxes (Ciais et al., 2022). The specific methodology used to calculate the budgets for CO_2, CH_4 and N_2O from each inversion system is

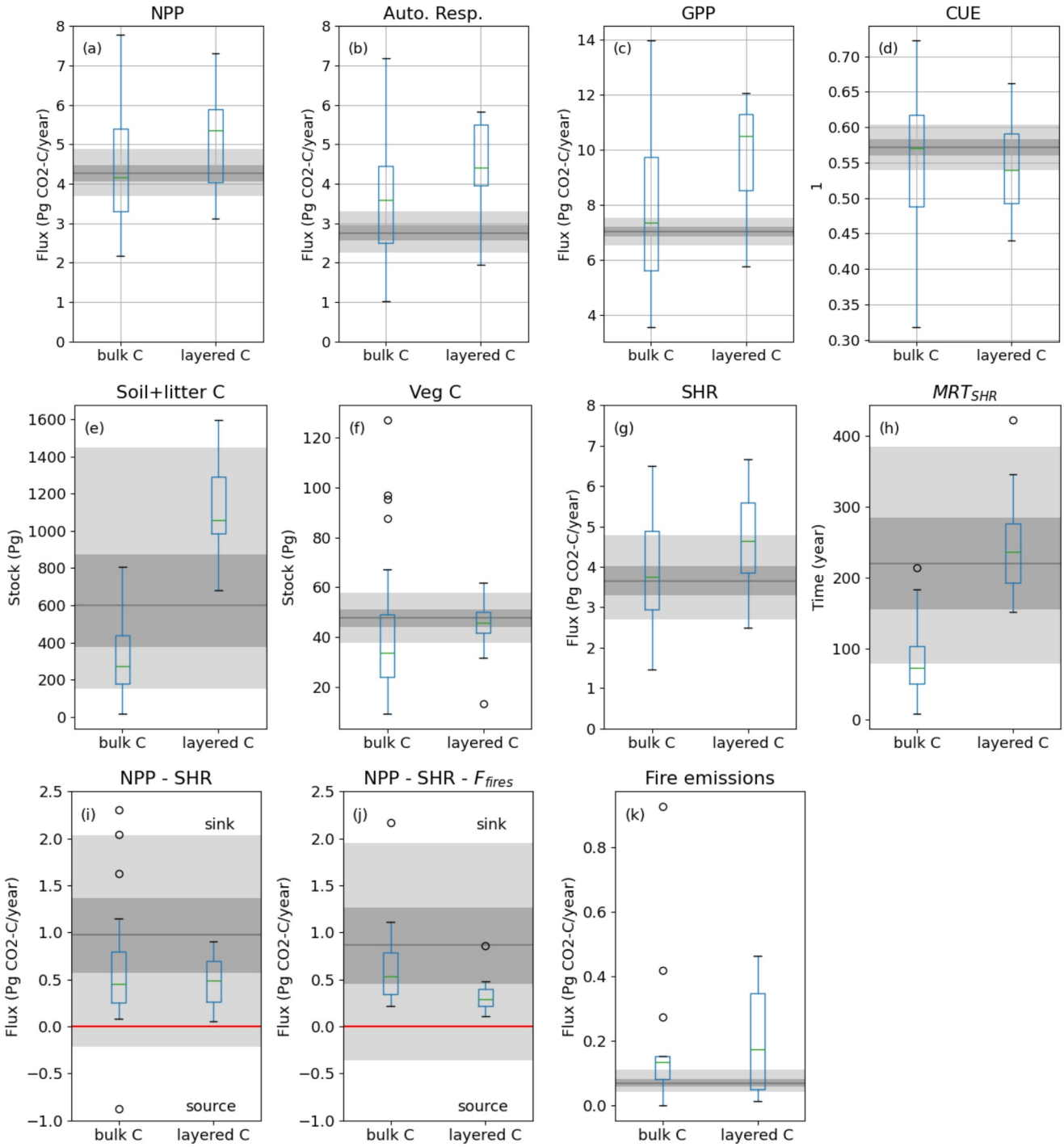

Figure 3. Carbon fluxes, stocks and relevant ecosystem properties from the process-based models listed in Table S1 in Supporting Information S1 over the BAWLD region. The top row shows (a) net primary productivity (NPP), (b) autotrophic respiration (R_a) (c) gross primary productivity (GPP), and (d) carbon use efficiency (CUE, dimensionless). The middle rows show (e)the sum of soil and litter carbon; (f) vegetation carbon; (g) heterotrophic respiration (SHR); and (h) the mean residence time of dead organic matter (MRT_{SHR}). The bottom row (i) the net ecosystem productivity (NPP -), (j) the net biosphere productivity (NPP–SHR–F_{fire}) and (k) the fire emissions. In each subplot, the left hand box plot ("*bulk* C," $n = 38$) is for models without permafrost carbon and the right hand box plot ("*layered* C," $n = 14$) is for models with permafrost carbon. The gray shading represents the likely range estimated by the observationally informed CARDAMOM analysis. The solid gray line indicates the 50% quantile, that is, the most likely estimate. The dark gray zone defines the 50% confidence interval around the 50% quantile, while the light gray zone is the 95% confidence interval around the 50% quantile. In the (NPP–SHR) and (NPP–SHR–F_{fires}) plots, the red line is at zero and positive values are a net uptake of carbon.

described in more detail in (Friedlingstein et al., 2022) for CO_2 (Saunois et al., 2020), for CH_4, and (Tian et al., 2020) for N_2O. The data were retrieved from the GCP/MPI-BGC/RECCAP-2 data portal (https://www.bgc-jena.mpg.de/geodb/) where the total number of inverse modeling estimates available was six for CO_2, 22 for CH_4 and three for N_2O. For CO_2, these six estimates have undergone a spatial adjustment for differences in the used fossil fuel, cement emissions and cement carbonation sink. One additional CO_2 flux estimate was added (Chandra et al., 2022) to make a total of seven models. Inversion estimates for CO_2 and CH_4 were derived from either in situ (surface) observations of atmospheric GHG mole fractions or satellite-derived total column estimates. Note that satellite estimates of CO_2 and CH_4 are available primarily from 2009 onwards, for example, from the Greenhouse gases Observing SATellite (GOSAT) (CO_2 and CH_4) and Orbiting Carbon Observatory-2 (OCO-2) (CO_2) missions. Among the 22 available estimates for CH_4, there were multiple submissions from the same group using different configurations of the atmospheric data or errors associated with the data. These submissions were first averaged and then the average estimate was used alongside estimates from the other groups. This resulted in 14 final inverse model estimates used to calculate the mean CH_4 budget. Of these, three inversions rely on GOSAT data. To assess whether systems relying on GOSAT data differed compared with those using surface station data we analyzed paired monthly means for all months were data was available using both GOSAT and surface data. Contrary to potential concerns that satellite systems underestimate fluxes at high latitudes due to lack of sunlight in winter (Pandey et al., 2016), we found that GOSAT inversions actually showed slightly higher mean monthly fluxes with differences between paired-runs of +13% and +22% for CTE and NTF-4DVAR-NIES, respectively. The third GOSAT-inversion (LMDZ-PYVAR) deviated by just a few percent from the CH_4 ensemble mean. This supports earlier findings suggesting that when satellite data are not available, the inversion framework tends to revert back to pre-specified prior flux estimates (Byrne et al., 2022). Based on these analyses, we find no reason to form separate inversion ensembles for satellite-augmented runs. Even though we find little evidence of systematic differences in systems using satellite derived observations, there is considerable variability between the analysis systems that come from the choice of prior flux estimates, choice of atmospheric transport model and/or other assumptions that go into constructing the inverse modeling framework. A comprehensive assessment of the accuracy of individual estimates is lacking for CH_4 and N_2O; but (Friedlingstein et al., 2022) provide an assessment of the skill of inversions against independent aircraft observations for CO_2 (for six out of the seven used here). We calculate the budget using the mean annual value from these ensembles of estimates. For estimates of N_2O, the estimates from one model system deviated by more than an order of magnitude from the other two systems. We were unable to diagnose why this model system estimated these very high fluxes, but because they lie outside the range of what can be reconciled with the global N_2O budget (Tian et al., 2020), the data were not used further. With these changes, the included number of inverse modeling estimates available were seven, 14 and two, for CO_2, CH_4 and N_2O, respectively (Table S2 in Supporting Information S1). There was a large variation in the spatial resolution of the inverse model systems. In all cases, the permafrost mask, which was available at ∼1°, was regridded to the resolution of the estimates from the individual models, then the flux estimates were sampled using the permafrost mask and finally averaged using area-weighting to generate a single value at monthly time steps for the permafrost study domain. This procedure follows the protocol outlined in previous RECCAP2 studies (Ciais et al., 2022). Data of mean monthly GHG fluxes across the full study domain for each specific inverse model used to calculate decadal means is available in Hugelius et al. (2024) as well as Tables S4, S5 and S6 in Supporting Information S1 (for CO_2, CH_4 and N_2O, respectively).

Top-down estimated fluxes of CO_2 from fires (not added to the total, reported as sub-flux) are extracted from a separate study combining satellite retrievals and atmospheric inversion of carbon monoxide (CO) converted to CO_2-C emissions using fixed emission factors (Zheng et al., 2023). Gridded estimates of fire CO_2-C fluxes from this study were retrieved (https://doi.org/10.6084/m9.figshare.21770624, resolution of 3.75° × 1.9°), clipped to the extent of our study domain and summarized for the relevant time periods. To report separate sub-fluxes of CH_4 from fires, data were extracted from the Global Methane Budget inventory using the Biomass and biofuel burning component of the top-down ensemble of global inversion estimates (Saunois et al., 2020) available for 2000–2017. These are inventory-based but methodologically consistent with the CH_4 inversions and reported together with the inversion data.

3. Results and Discussion

3.1. Bottom-Up Budgets From Models and Upscaling

3.1.1. Ecosystem CO_2 Budgets From Process-Based Models

The land surface area in the permafrost region is estimated to be a net sink of CO_2 by both model ensembles (including (layered C) or excluding (bulk C) representation of permafrost C) and the CARDAMOM analysis (Table 2). When considering net ecosystem productivity (NPP–SHR), the full model ensemble suggests a net sink of −450 (−110 to −1,370) Tg CO_2-C yr^{-1} with CARDAMOM showing a net sink of −960 (sink of −1880 to source of 20) Tg CO_2-C yr^{-1} (Table 2). Out of the 52 process-based model runs, 26 runs did not include fire and as a result are excluded from the net biome productivity (NPP–SHR–F_{fire}) reported (Table S1 in Supporting Information S1). The 26 models that include fire, albeit not including combustion of belowground sources, estimate fire emissions of 130 (20–460) Tg CO_2-C yr^{-1}. The estimate including fire is larger and has a much greater spread than CARDAMOM (60 (50–100) Tg CO_2-C yr^{-1}). In the model sub-ensemble ($n = 14$) that includes permafrost processes as well as fire, the estimated fire emissions are higher (170 (20–460) Tg CO_2-C yr^{-1}), reducing the net land uptake to −290 (−120 to −630) Tg CO_2-C yr^{-1} (Table 2). In CARDAMOM, inclusion of fires reduces the estimated net land uptake to −870 (−1,780 to 160) Tg CO_2-C yr^{-1} (Figure 3j and Table 2). Although not reflected in the model ensembles, CARDAMOM's ensemble shows that the source/sink boundary falls between the 75th and 90th quantiles, and thus the permafrost region could also be a small net source of C in CARDAMOM. The models within the process-based model ensemble were run for several different model intercomparison projects, so they are not directly comparable in terms of protocol or time period covered. A more constrained ensemble may reduce the uncertainties in the budget estimates. However, the spread of model estimates is still smaller than that from the observationally informed CARDAMOM assessment.

In terms of the vegetation C fluxes (i.e., NPP, Autotrophic respiration, GPP and CUE; Figures 3a–3d), there is no significant difference (Mann-Whitney, $p < 0.01$) between the layered C models and the bulk C models. CARDAMOM's data-informed analysis falls within the spread of the process models. However, the spread of values simulated by the process models is much larger than that suggested by CARDAMOM. This is in contrast to the net ecosystem and net biome productivity fluxes discussed above.

The MRT_{SHR} is significantly longer in models with explicit permafrost C (247 years, layered C) than those without (85 years, bulk C) (Mann-Whitney $p < 0.01$; Figure 3h). Longer MRT_{SHR} in layered C models more closely aligns with CARDAMOM's observationally informed analysis. Furthermore, the overall majority of the layered C models fall within CARDAMOM's 95% CI. The ones that fall outside have a longer MRT_{SHR} than CARDAMOM. In contrast, only a small fraction of the bulk C models are consistent with the CARDAMOM MRT_{SHR} with the remainder of the models having a shorter MRT_{SHR} than CARDAMOM. The layered C models also have a significantly larger soil C stock, which combined with the differences in MRT_{SHR} leads to simulating regional heterotrophic respiration similar to the bulk C models. It is expected that the heterotrophic respiration is similar between the two model ensembles–the additional soil carbon that has been added in the deeper layers is mostly frozen and therefore has very small heterotrophic respiration rates. Thus, the bulk of C models estimate regional heterotrophic respiration that is consistent with both CARDAMOM and layered C models, but the layered C models have the potential for large changes in respiration in the future, whereas the bulk C models do not.

3.1.2. Wetland CH_4 Fluxes From Process-Based Models

Full model ensemble budgets are only available for CO_2, but for CH_4, a process-based model ensemble ($n = 13$) of natural wetland CH_4 flux estimates was available (Saunois et al., 2020). The ensemble annual mean is a wetland CH_4 source of 12 (8.6, 16) Tg CH_4-C yr^{-1} (Table 2). The interannual variability of the ensemble is low (annual means between 11.2 and 14.1), but with a large spread within the model ensemble; annual means over the period varied from 4.9 to 28 Tg CH_4-C yr^{-1} for individual models (see Table S2 in Supporting Information S1 for more details).

3.1.3. Ecosystem GHG Budgets From Data Driven Upscaling

Bottom-up estimates of GHG budgets from data driven upscaling are based on Ramage et al. (2024) and summarized in Table 3. All numbers are annual means estimated over the full reporting period of 2000–2020.

Table 3
Summary of All Main Budget Posts for the Three GHGs (Annual Mean and 95% CI) From Bottom-Up Ecosystem Upscaling as Presented by Ramage et al. (2024)

		CO_2	2.5% CI	97.5% CI	CH_4	2.5% CI	97.5% CI	N_2O	2.5% CI	97.5% CI
	Surface area 10^{-6} km^2	Tg CO_2-C yr^{-1}			Tg CH_4-C yr^{-1}			Tg N_2O-N yr^{-1}		
Data-driven upscaling (All numbers from Ramage et al. in prep)										
Total budget	**17.05**	**12**	−606	661	**38**	22	53	**0.7**	0.1	1.2
Sum all terrestrial land cover:		−340	−836	156	25.6	14.69	36.4	0.55	−0.03	1.14
Sum uplands	14.2	−267	−687	153	1.0	−2.6	4.5	0.37	0.03	0.72
Boreal forests	9	−270	−540	−0.9	−1.1	−2.2	0.0	0.14	−0.01	0.3
Dry tundra	5.2	2.9	−148	154	2.1	−0.4	4.5	0.23	0.04	0.42
Sum wetlands	2.8	−72	−148	3.7	25	17	32	0.18	−0.06	0.42
Permafrost-free wetlands	1.6	−69	−125	−14	21	14	27	0.07	−0.03	0.17
Permafrost bogs	0.86	−0.05	−0.8	0.73	0.7	0.29	1.1	0.10	−0.03	0.23
Tundra wetlands	0.4	−2.7	−23	17	3.3	2.7	3.9	0.01	0.00	0.02
Fires	1.1	121	97	145	1.8	1.4	2.1	0.12	0.10	0.15
Inland waters	1.4	231	132	360	9.4	4.5	13.1	0.002	0.001	0.003
Geological emissions		NA	NA	NA	1.5	1.2	1.8	NA		

Note. Bold values indicate the net ecosystem GHG balances used for annual budgets.

The total budget of CO_2 is near neutral, but with a large uncertainty range (12 (−606, 661) Tg-CO_2-C yr^{-1}; Table 3). Sinks of CO_2, mainly in Boreal forest (−270 (−540, −1) Tg-CO_2-C yr^{-1}) and Permafrost-free wetland land cover types (−69 (−125, −14) Tg-CO_2-C yr^{-1}) are offset by sources of CO_2 from fires (121 (97, 145) Tg-CO_2-C yr^{-1}) and Inland waters (streams, rivers, lakes and ponds combined; 231 (132, 360) Tg-CO_2-C yr^{-1}). The land cover types Dry tundra ecosystems, Permafrost bogs and Tundra wetlands have CO_2 budgets within ±3 Tg of neutral.

The total bottom-up data driven budget for CH_4 shows a net source of 38 (22, 53) Tg CH_4-C yr^{-1} (Table 3). The strongest CH_4 sources are permafrost-free wetlands and inland waters (21 (14, 27) and 9.4 (4.5, 13) Tg CH_4-C yr^{-1}, respectively). All other land cover types, as well as fires and geological emissions, represent weak sources of CH_4 to the atmosphere (from 1.2 to 3.3 Tg CH_4-C yr^{-1}), with the exception of Boreal forests, which are a weak sink (−1.1 (−2.2, 0) CH_4-C yr^{-1}).

The total bottom-up data driven budget for N_2O shows a net source of 0.7 (0.1, 1.3) Tg N_2O-N yr^{-1} (Table 3). All land cover types and fires represent net sources of N_2O to the atmosphere, but with very large uncertainty. The strongest sources are Boreal forest and Dry tundra ecosystems (0.14 (−0.01, 0.3) and 0.23 (0.04, 0.42) Tg N_2O-N yr^{-1} respectively).

3.1.4. Integrated Bottom-Up Budget

The integrated bottom-up for CO_2 shows a combined sink in upland ecosystems and wetlands from ecosystem upscaling that is somewhat lower than the process-based model ensemble estimate (−218 and −302 Tg-CO_2-C yr^{-1}, respectively). When adding inland water fluxes, the integrated bottom up estimate for CO_2 is a weak sink with a wide uncertainty range on either side of a neutral budget (−29 (−709, 455) Tg-CO_2-C yr^{-1}). For CH_4, the combined sum of data-driven ecosystem types and fires is similar to the combined wetland process-based models plus wetland abrupt thaw fluxes (28 and 29 Tg CH_4-C yr^{-1}, respectively). When adding inland water fluxes, the integrated bottom up estimate for CH_4 is a source of 39 (23, 53) Tg-CH_4-C yr^{-1}. For N_2O, only the data-driven upscaling estimate is available, and this is used as a best estimate for the bottom-up budget (a sink of 0.7 (0.1, 1.3) Tg N_2O-N yr^{-1}).

3.2. Top-Down Atmospheric Inversion Budgets

The ensemble of atmospheric inversion models for CO_2 (n = 7) indicates, for all members, that the permafrost region is a net CO_2 sink with a multi-annual mean of −587 (−862, −312) Tg-CO_2-C yr^{-1} (2000–2020, excluding

Table 4
Summary of the Different Budget Components (Annual Mean and 95% CI) Used to Generate an Integrated Bottom-Up Budget for All Three GHGs

		CO_2	2.5% CI	97.5% CI	CH_4	2.5% CI	97.5% CI	N_2O	2.5% CI	97.5% CI
		Tg CO_2-C yr^{-1}			Tg CH_4-C yr^{-1}			Tg N_2O-N yr^{-1}		
Data-driven synthesis	Total budget	12	−606	661	38	22	53	0.67	0.07	1.29
	Sum upland landcover types	−267	−687	153	1	−2.6	4.5	0.37	0.03	0.72
	Sum wetlands	−72	−148	4	25	17	32	0.18	−0.06	0.42
	Fires	121	97	145	1.8	1.4	2.1	0.12	0.10	0.15
	Inland waters	231	132	360	9.4	4.5	13	0.002	0.001	0.003
Abrupt thaw wetland flux	(not included in data-driven upscaling total)	19	13	26	19	12	26			
Process-based models	Model ensemble NEE (NPP- SHR–Ffire)	−350	−1,040	−150	NA			NA		
	Model ensemble CH4 wetland flux	NA			12	8.6	16	NA		
Integrated bottom-up budget	Natural ecosystems (including fires)	−29	−709	455	39	23	53	0.67	0.07	1.29
	Mean vegetated upland + wetland ecosystems (with fire)	−260	−841	95	29	18	40	NA		
	Data-driven, sum upland + wetland landcover types	−218	−738	302	28	16	39	0.67	0.07	1.29
	Model ensemble NEE and wetland abrupt thaw	−302	−943	−112	NA			NA		
	Model ensemble wetland CH_4 flux and abrupt wetland thaw				31	21	42			
	Inland waters (from data-driven synthesis)	231	132	360	9.4	4.5	13	0.002	0.001	0.003

anthropogenic fluxes; Table 5). This estimate accounts for CO_2 sources from fires, estimated by one inverse model system as 78 (51, 104) Tg-CO_2-C yr^{-1}. The inversion systems show a slightly stronger mean annual sink in 2010–2020 compared to 2000–2009 (−643 (−917, −369) and −526 (−802, −250) Tg-CO_2-C yr^{-1}, respectively). But this change is small compared to the range.

The ensemble of inversion models analyzing CH_4 (n = 14) shows a multi-annual mean source from natural ecosystems of 15 (11, 18) Tg CH_4-C yr^{-1} (2000–2017; Table 5). This estimated source includes small fluxes from fires (1.4 (1.2, 1.6) Tg CH_4-C yr^{-1}). There is no notable difference between the first and second decade.

For N_2O, only two separate inverse model estimates are available and they show a neutral balance or weak source of N_2O, with a multi-annual mean of 0.09 (−0.19, 0.37) Tg N_2O-N yr^{-1} (Table 5). The N_2O source was weaker in 2010–2019 compared to 2000–2009 (Table 5).

Table 5
Summary Table of GHG Emissions (Annual Mean and 95% CI) From the RECCAP2 Permafrost Domain From Atmospheric Inversion Models

	Tg CO_2-C yr^{-1}	2.5% CI	97.5% CI	Tg CH_4-C yr^{-1}	2.5% CI	97.5% CI	Tg N_2O-N yr^{-1}	2.5% CI	97.5% CI
Inversion ensemble 2000–2009*	−526	−802	−250	14	11	18	0.01	−0.24	0.27
Fire sub-flux**	*73*	*48*	*98*	*1.2*	*1.0*	*1.5*	*NA*		
Inversion ensemble 2010–2020*	−643	−917	−369	15	12	18	0.16	−0.14	0.46
Fire sub-flux**	*82*	*54*	*110*	*1.6*	*1.4*	*1.7*	*NA*		
Inversion ensemble 2000–2020*	−587	−862	−312	15	11	18	0.09	−0.19	0.37
Fire sub-flux**	*78*	*51*	*104*	*1.4*	*1.2*	*1.6*	*NA*		

Note. The reported inverse model fluxes are the ecosystem fluxes, not including anthropogenic emissions. Sub-fluxes from fires (already included in the total) are also shown for CO_2 and CH_4. *GHG are reported for different periods: 2000–2020 for CO_2, 2000–2017 for CH4, and 2000–2019 for N_2O. **Fire sub-flux of CO_2 from Zheng et al. (2023) CI range assumed to be proportional to reported CI for trends in that paper. Fire sub-flux of CH_4 is biomass and biofuel burning extracted by mask from global methane budget data sets used in Saunois et al. (2020).

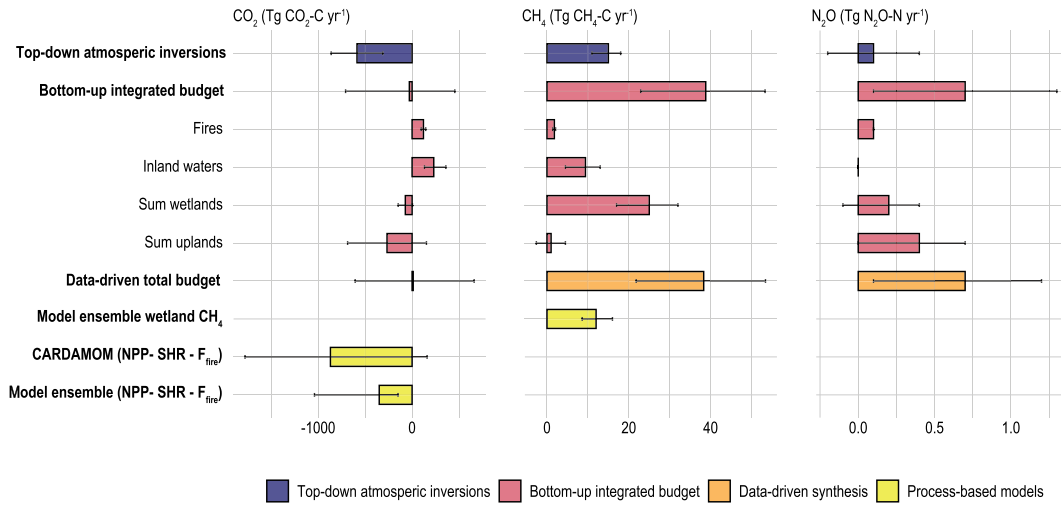

Figure 4. Summary of main budget items for all 3 GHGs over the time period 2000–2020 calculated using different methods. The error bars represent the 95% confidence interval.

There are no previous studies synthesizing atmospheric inversion model estimates of these three GHGs for permafrost regions, but our results are consistent with studies of similar scope. A Tundra biome synthesis from the first generation of RECCAP (McGuire et al., 2012) estimated a net CO_2 sink (-120 Tg C yr^{-1}) between 2000 and 2006 but with very large differences between individual model estimates in the ensemble (range -440, $+210$). Since then, more global top-down inverse GHG flux estimates have become available (Friedlingstein et al., 2022), and some recent studies have provided GHG budgets for northern regions. Bruhwiler et al. (2021) analyzes inverse model ensembles across Boreal (50–60° N) and Arctic (60–90° N) domains and estimated CO_2 sinks (-290 and -130 Tg CO_2-C yr^{-1}, respectively for 1980–2017) and CH_4 sources (16 and 9 Tg CH_4-C yr^{-1}, respectively for 2000–2017). Using a similar time series of estimates from atmospheric inversion models, Liu, Kuhn, et al. (2022) find that the permafrost region changed from being CO_2 neutral (1980–2000) to a CO_2 sink in 2000–2017 (ca. -200 ± 100 Tg CO_2-C yr^{-1}). There are no previous atmospheric inverse modeling estimates of N_2O specifically for the permafrost region with which we can compare our results. A recent global N_2O inversion (Stell et al., 2022) estimated sources of 3–4 Tg N_2O-N yr^{-1} between latitudes 30–90°N. But since this area stretches far outside our study region, and contains areas with strong agricultural sources of N_2O, direct comparison with our study is not suitable.

3.3. Comparison of Bottom-Up and Top-Down Budgets

Synthesis and comparison of the different methods show both convergence and divergence in the different GHG budgets (Figures 4 and 5). Below, the bottom-up and top-down budgets for individual GHGs are compared and discussed (excluding anthropogenic and lateral fluxes).

3.3.1. Budgets of CO_2

The CO_2 budget for natural ecosystems (excluding anthropogenic fluxes) using bottom-up approaches is a weak sink of -29 (-709, 455) Tg CO_2-C yr^{-1}, while atmospheric inversion models show a much stronger sink of -587 (-862, -312) Tg CO_2-C yr^{-1} (Table 6, Figure 5). The 95% CI range of the bottom-up budget is large and spans across the top-down budget, while the range of the top-down budget is narrower and indicates a clear CO_2 sink. In comparison to top-down and bottom-up budgets, the observationally constrained CARDAMOM system (Figure 3, Table 2) estimates a stronger sink of CO_2 -870 (-1780, 160) Tg CO_2-C yr^{-1}, but CARDAMOM's ensemble estimate crosses the source/sink boundary between the 75th and 90th quantile and may be consistent with the other bottom-up sources. Especially for the Tundra biome, process-based models (and CARDAMOM) have CO_2 budgets close to neutral, in line with data-driven upscaling for terrestrial land cover types in that region. Altogether, bottom-up and top-down approaches both show a sink of CO_2 in the region, but of different magnitude, and with some ensemble members not excluding a weak source.

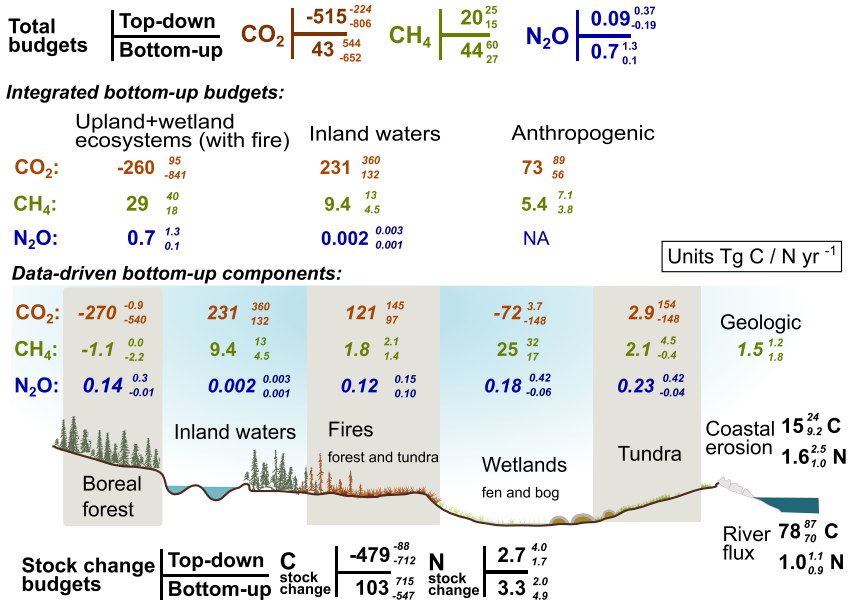

Figure 5. Overview of mean estimated budgets and fluxes. The top panel shows top-down and bottom-up for all three GHGs, with total budgets calculated as natural ecosystem budgets plus anthropogenic emissions. Below this, the integrated bottom-up budget as well as anthropogenic emissions are presented separately, followed by estimated mean GHG and lateral fluxes from data-driven assessments for different land cover types or processes. Stock changer budgets (not including anthropogenic emissions or trade fluxes) are shown at the bottom. All numbers are shown in the units Tg C or N per year.

In this paper, we present a top-down view with no analyses of spatial patterns in individual or ensemble inversion models. This lack of spatial information makes it difficult to pinpoint the sources of discrepancies between top-down and bottom-up approaches. However, the flux components can be compared for the two methods used to construct CO_2 budgets. Boreal forest and wetland ecosystems are consistent sinks across the bottom-up approaches, but this sink is offset by fluxes from inland waters and fires. Only data-driven upscaling approaches are available to estimate inland water fluxes, which are typically not represented in process-based models. If inland waters are excluded from ecosystem upscaling, the net budget for terrestrial land cover types, including fires, is very similar to the net ecosystem productivity (NPP–SHR–F_{fire}) flux of process models with layered soil C pools (Table 4 and Figure 3). This suggests that the CO_2 budget for these ecosystems agrees with the observational data sets and the models which explicitly represent soil layers and permafrost. This further suggests that process-based models would potentially project a weaker CO_2 sink with a better representation of inland waters. The separate methods for calculating CO_2 fire fluxes spread with estimates of 130, 60, 77 and 121 Tg CO_2-C yr^{-1}, from process-based models, CARDAMOM, one atmospheric inversion, and the bottom-up estimate, respectively. Comparison of different inventories and process-based models in this paper shows that fluxes not represented in the process-based models are potentially large and should be targeted for inclusion in models. In addition to natural ecosystem fluxes, there may be geological sources of CO_2 that we do not account for, as no separate estimates are available from the permafrost region. The full global geological CO_2 emissions are estimated to be 160 Tg CO_2-C yr^{-1} (Mörner & Etiope, 2002), and it is likely that a small fraction of those fluxes occur within our study region, but are unaccounted for in this budget.

3.3.2. Budgets of CH_4

For the natural balance of CH_4 (excluding anthropogenic fluxes), both the integrated bottom-up budget and the top-down atmospheric inversion models consistently show a source, albeit of different magnitudes at 39 (23, 53) and 15 (11, 18) Tg CH_4-C yr^{-1}, respectively (Table 6, Figure 5). Even though both the bottom-up and top-down methods show a source of CH_4, their uncertainty ranges do not overlap, suggesting that there may be a systematic bias between the methods.

In the data-driven upscaling, fluxes of CH_4 are characterized by high fluxes per areal unit from wetlands and some lakes types. Other classes with more extensive areal coverage, such as Boreal forests and Dry tundra, are neutral

Table 6
Summary of All Main Budget Posts (Annual Mean and 95% CI) for the Three GHGs, Including Anthropogenic Fluxes As Well As Lateral Fluxes and Total Stock Changes of C and N

	CO_2	2.5% CI	97.5% CI	CH_4	2.5% CI	97.5% CI	N_2O	2.5% CI	97.5% CI
	Tg CO_2-C yr^{-1}			Tg CH_4-C yr^{-1}			Tg N_2O-N yr^{-1}		
Natural ecosystems (including fires)									
Bottom-up integrated budget	−29	−709	455	39	23	53	0.7	0.1	1.3
Top-down atmospheric inversions	−587	−862	−312	15	11	18	0.09	−0.19	0.37
Anthropogenic emissions									
Total budget	73	56	89	5.4	3.8	7.1	NA		
Fossil fuels	73	56	89	4.9	3.3	6.5	NA		
Agriculture and waste	NA			0.54	0.44	0.64	NA		
Total budgets (natural ecosystems and anthropogenic emissions)									
Bottom-up integrated budget	43	−652	544	44	27	60	NA		
Top-down atmospheric inversions	−515	−806	−224	20	15	25	NA		

	Carbon stock changes			Nitrogen stock changes		
	Tg C yr^{-1}	2.5% CI	97.5% CI	Tg N yr^{-1}	2.5% CI	97.5% CI
Mean gas C (CO_2+CH_4) and N (N_2O) budgets						
Bottom-up	10	−626	604	0.7	0.1	1.3
Top-down	−573	−791	−199	0.09	−0.19	0.37
Lateral flux C and N budgets	94	79	111	2.6	1.9	3.6
Riverine flux	78	70	87	1.0	0.9	1.1
Coastal erosion	15	9.2	24	1.6	1.0	2.5
Sum C and N stock changes						
Bottom-up	103	−547	715	3.3	2.0	4.9
Top-down	−479	−712	−88	2.7	1.7	4.0

or even weak sinks due to oxidation and uptake of atmospheric CH_4 occurring in these drier soils. Land cover types with high CH_4 emissions are often spatially heterogeneous (with large uncertainties in total area of classes) and sometimes emissions can be especially large along the margins of these land cover patches. These conditions make CH_4 challenging to upscale, and it also means that the spatial landscape heterogeneity and the spatial resolution of upscaling or modeling become very important for determining accurate budgets (Treat, Marushchak et al., 2021). For inverse models, this scale issue should not have large effects on how the frameworks adjust between prior and posterior fluxes, but the resolution and magnitude of the prior flux ensembles may affect the budget.

There are no process-based model CH_4 budgets for the full permafrost region landscape, but for wetlands, a model ensemble ($n = 13$) estimates a CH_4 source of 12 (8.6, 16) Tg CH_4-C yr^{-1}. This wetland source is circa half of the data-driven ecosystem upscaling estimates of combined wetland flux of 25 (17, 32) Tg CH_4-C yr^{-1}. Much of this difference may be explained by the lack of abrupt thaw wetlands in the models, which are included among data-driven land cover types, and the integrated bottom-up budget. In addition, the discrepancy may be partly explained by the poor representation of cold-season CH_4 emissions in process-based models, which tend to be underestimated relative to field-based observations (Treat, Marushchak, et al., 2018). The large differences between estimates suggest that future development of process-based model estimates should target the inclusion of inland waters, abrupt thaw, and processes related to atmospheric CH_4 consumption in upland ecosystems.

3.3.3. Budgets of N_2O

For N_2O, both the bottom-up ecosystem flux upscaling and the top-down atmospheric inversion models show a net source to the atmosphere, but with large differences between estimates (0.7 (0.1, 1.3) and 0.09 (−0.19, 0.37)

Tg N_2O-N yr^{-1}, respectively) (Table 6, Figure 5). Both methods have relatively wide uncertainty ranges that overlap each other, and the inverse model estimates cannot be distinguished with confidence from a neutral budget. The bottom-up estimates are seven times higher than the top-down estimates, demonstrating a clear need to refine the methods and gather more observational data. The high bottom-up budget is mainly driven by fluxes from large areas of upland Dry tundra and Boreal forest (despite relatively small fluxes per unit area). Uncertainty ranges are wide for all land cover classes and the mean values for classes may be driven up by preferential reporting from measurement sites with high fluxes such as thaw features or barren ground, particularly in permafrost peatlands (Repo et al., 2009; Yang et al., 2018).

Tian et al. (2020) presented a global quantification of N_2O sources and sinks, where top-down and bottom-up estimates were very similar (ca. 17 Tg N_2O-N yr^{-1}) Although they do not present numbers specifically by biome, the estimates for northern regions in Tian et al. (2020) are generally low, and more consistent with our top-down estimates. We provide no process-model ensemble estimates for N_2O, as few process-based models simulate cycling of N_2O in permafrost ecosystems. One exception is a recent model-based study estimating an average mean annual flux of 4 mg N_2O-N m^{-2} yr^{-1} across several tundra ecosystem sites (Lacroix et al., 2022). If upscaled to the full tundra domain (5.58 M km^2 including the classes Wet tundra and Dry tundra), this would yield an annual flux of 0.022 Tg N_2O-N yr^{-1}, an order of magnitude lower than our bottom-up estimates for these same classes. This underscores that the uncertainty of the N_2O budget for the permafrost region is still large and that process-based N_2O modeling is in its infancy.

3.4. Anthropogenic CO_2 and CH_4 Emissions, Lateral Export and Total Stock Changes of C and N

Separate estimates of anthropogenic emissions are available from global gridded data for CO_2 and CH_4 (Table 6, see Table S7 in Supporting Information S1 for more details). For both gases, the emissions are dominated by combustion of fossil fuels occurring within the permafrost region. Anthropogenic emissions of CO_2 are estimated to be 73 (56, 89) Tg-CO_2-C yr^{-1}, mainly from gas and oil (26 (19, 34) and 32 (27, 36) Tg-CO_2-C yr^{-1}, respectively) (Table S7 in Supporting Information S1). Anthropogenic emissions of CH_4 are estimated to be 5.3 (3.8, 6.7) Tg-CH_4-C yr^{-1}, mainly from fossil fuels but with a small contribution from agriculture and waste (4.7 (3.4, 6.0) and 0.54 (0.43, 064) Tg-CH_4-C yr^{-1}, respectively) (Table S7 in Supporting Information S1). These anthropogenic fluxes have not been included in the bottom-up and top-down budgets reported above, but are included in the calculation of the full combined Global Warming potential of all three GHGs.

3.5. Lateral Export and Total Stock Changes of C and N

In addition to the natural and anthropogenic GHG exchange with the atmosphere, C and N are laterally exported from the permafrost region to the Arctic Ocean via riverine transport and coastal erosion (Table 6). The lateral fluxes of organic C were estimated at 94 (79, 110) Tg C yr^{-1}, with riverine transport of DOC contributing 78 (70, 87) Tg C yr^{-1} and coastal erosion of soil and sediment organic C contributing 15 (9, 24) Tg C yr^{-1}. Lateral export of N from the permafrost region is estimated to be 2.6 (1.9, 3.6) Tg N yr^{-1} with a smaller component of riverine transport (1.0 (0.9, 1.1) Tg N yr^{-1}) compared to coastal erosion (1.6 (1.0, 2.5) Tg N yr^{-1}). The ratio of C:N lost via riverine transport is very high (ca. 80), while the C:N ratio in material lost via coastal erosion (ca. 10) is consistent with mature mineral soil organic matter in the permafrost region (Harden et al., 2012).

Combining the net CO_2 and CH_4 budgets (excluding anthropogenic fluxes) with lateral flux yields annual estimated organic C stock change budgets in natural ecosystems. The sign and magnitude of combined organic C stock change budgets depend on whether bottom-up or top-down approaches to GHG budgeting are used (103 (−547, 71) and −479 (−712, −88) Tg C yr^{-1}, respectively). Because we do not account for all N fluxes, we cannot close the full N budget, but we estimate N stock change based on the sub-set of fluxes we include. Our combined N_2O and lateral flux data spreads less between bottom-up and top-down approaches than for C. The mean estimate shows a net N loss to the atmosphere and ocean of 3.0 (1.8, 4.4) Tg N yr^{-1} (Table 6). As there is likely a net sink of C in the region, and the overall ecosystem C:N (in soil and vegetation) is unlikely to grow increasingly wider, we expect that if a fully closed N budget is available, a net source of N is more likely. This suggests a source of N into the system not quantified in our budgets. If we assume a C stock change as the mean of bottom-up and top-down and that the total ecosystem C:N ratio (for vegetation and surface soils) is stable over time at a value around 15–20 (Palmtag et al., 2022), a total N input to the ecosystem of 11–14 Tg N yr^{-1} would be needed to balance the N stock change budget in relation to the C stock change budget. Missing N sources needed to balance the budget may be

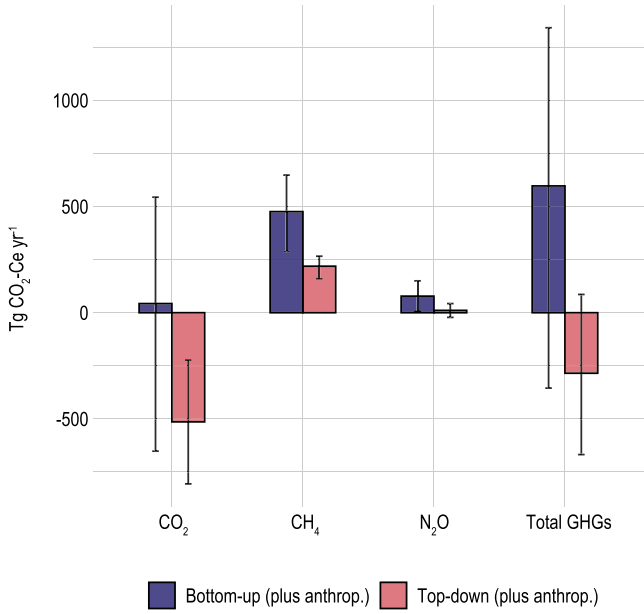

Figure 6. Annual global warming potential from GHG budgets for bottom-up and top-down approaches. Includes all ecosystem fluxes, and anthropogenic fluxes (CO_2 and CH_4 only). All numbers were converted to CO_2-equivalents (Tg CO_2-Ceq, with 95% CI) using a 100-year Global Warming Potential (GWP-100). Table 7 complements this figure by showing more detailed sub-fluxes for the different categories.

atmospheric N deposition or biological N_2 fixation, both important sources of available N for subarctic and arctic ecosystems (Rousk et al., 2018; Yuan et al., 2023). Yuan et al. (2023) reported an estimated N deposition between 10 and 15 Tg N yr^{-1} for the pan-Arctic, in close agreement with the fluxes needed to close the budget. Mean N_2 fixation rates of boreal forest (0.12 g N m^{-2} yr^{-1}) and tundra ecosystems (0.33 g N m^{-2} yr^{-1}) (Yu & Zhuang, 2020) would yield additional N sinks of 1.2 and 2.1 Tg N yr^{-1}, respectively, if upscaled to the full spatial extent of the Boreal forests and Tundra biomes within the permafrost region. Although these estimates of additional N sinks into ecosystems are uncertain, they suggest that our estimated net loss of N via N_2O flux and lateral losses from the domain are a small component of the N cycle, and that a balanced full N-budget would be in agreement with an organic C stock change budget based on average GHG flux and lateral C flux.

3.6. Combined Global Warming Potential of the Permafrost Region

A general budget overview shows a significant spread between bottom-up and top-down estimates for all three gases (Figure 5). The bottom-up approaches consistently estimate stronger GHG sources (or weaker sinks) compared to top-down atmospheric inversions. Using a common unit of CO_2-C equivalents over 100 years (GWP100), and including both ecosystem and anthropogenic fluxes, the net balance of the 3 GHGs from bottom-up approaches shows a net source of 597 (−355, 1,342) Tg CO_2-C eq yr^{-1} while top-down atmospheric inversions show a sink of −285 (−668, 86) Tg CO_2-C eq yr^{-1} (Figure 6, Table 7). The CO_2 budgets are close to neutral or a sink in bottom-up and top-down budgets, respectively, while CH_4 and N_2O are consistent, but varying, sources of Global Warming Potential (Figure 6, Table 7). Methane is of particular importance to the full Global Warming Potential, highlighting the importance of monitoring non-CO_2 trace gases. Because of their different properties, life times and concentrations in the atmosphere, the total radiative balance of the three GHGs together varies depending on the timescale. Therefore, the estimates of the combined GHG sink or source strengths based on GWP calculations should be interpreted with

Table 7
Summary of Annual GHG Budgets for All Main Budget Posts, Converted to Mean CO_2-Equivalents (Tg CO_2-C_{eq}, With 95% CI) Using a 100-Year Global Warming Potential (GWP-100) From Bottom-Up Approaches, Top-Down Atmospheric Inversion Models and From Anthropogenic Fluxes

	CO_2	2.5% CI	97.5% CI	CH_4	2.5% CI	97.5% CI	N_2O	2.5% CI	97.5% CI	Total GHGs	2.5% CI	97.5% CI
GWP100	Tg CO_2-Ce yr^{-1}			Tg CO_2-Ce yr^{-1}			Tg CO2-Ce yr^{-1}			Tg CO_2eq yr^{-1}		
Natural ecosystems (including fires)	−29	−709	455	419	247	576	78	7.9	150	468	−453	1181
Mean vegetated upland + wetland ecosystems (with fire)	−260	−841	95	317	199	435	NA			57	−642	531
Data-driven, sum upland + wetland landcover types	−218	−738	302	300	171	417	78	7.9	150	160	−560	870
Model NEE and wetland abrupt thaw	−302	−943	−112	NA			NA			−302	−943	−112
Model wetland CH4 flux and abrupt wetland thaw				335	227	454				335	227	454
Inland waters (from data-driven synthesis)	231	132	360	102	49	140	0.23	0.12	0.35	333	181	501
Fires (from data-driven synthesis)	109	80	136	13	10	16	8.2	7.0	9.3	130	97	162
Natural ecosystems (including fires)	−587	−862	−312	162	119	194	11	−22	43	−414	−765	−74
Fires (from one inversion system)	78	51	104	NA			NA			78	51	104
Fossil fuel, agriculture and waste, cement	73	56.3	88.74	57	41	72				129	98	161
Bottom-up plus anthropogenic	43	−652	544	476	289	648	78	8	150	597	−355	1,342
Top-down plus anthropogenic	−515	−806	−224	219	160	266	11	−22	43	−286	−668	86

Note. A GWP-100 of 29.8 for CH_4 and 273 or N_2O relative to CO_2 was used (Forster et al., 2021; Table 7.15).

care. Using CO_2-C equivalents over a shorter time-scale of 20 years (GWP20) yields net sources from both bottom-up and top-down approaches (1,361 (168, 2,512) and 81 (−399, 533), Tg CO_2-C eq yr^{-1} respectively) (Table S8 in Supporting Information S1). Over multiple centuries (GWP500), the bottom-up estimate remains a source, but the top-down sink is stronger (196 (−579, 772) and −451 (−789, −116) Tg CO_2-C eq yr^{-1}, respectively) (Table S8 in Supporting Information S1).

The uncertainty ranges of the combined GHG budgets (using GWP100), in both bottom-up and top-down approaches, span across a neutral budget. Because the budget is so close to neutral, recent and future shifts in disturbance regimes may shift the sign of the net GHG budget. The combined effect of fire (from bottom-up scaling) is a source of ca 120 Tg CO_2-Ceq yr^{-1} but unusually strong fire years can significantly increase the net GHG source. For instance, in the summer of 2021, global boreal fire emissions were nearly three times larger than the 2000–2020 mean (Zheng et al., 2023). Emissions of CO_2, CH_4, and N_2O from abrupt thaw landforms, both at present and in the future, are a large but highly uncertain source of GHGs. Abrupt thaw (thermokarst) may expand or shift rapidly over time and can be triggered by fires or by unusually warm summers (Turetsky et al., 2020). The estimated fluxes from abrupt thaw lakes and wetlands are conservative in the bottom-up data driven upscaling used for this assessment, but they may be as large as 300 CO_2-Ceq yr^{-1} for the 2000–2020 period (Ramage et al., 2024).

3.7. Main Sources of Uncertainties Within and Between GHG Budgets

For all three GHGs, bottom-up estimates consistently yield stronger radiative forcing sources than top-down estimates (Figures 4–6). Combined for all 3 GHGs over natural ecosystems, the bottom-up ecosystem scaling predicts a source of 468 (−453, 1181) Tg CO_2-Ceq yr^{-1} while the top-down inversions estimate a sink of −414 (−765, −74) Tg CO_2-Ceq yr^{-1} (Table 7, excluding anthropogenic fluxes). Both the systematic discrepancies between bottom-up and top-down methods, and the wide uncertainty ranges of data and model estimates point to a need for further refinement of methods, process representation and additional observational data. The two different sources for bottom-up budgets (data-driven upscaling and process-based models) agree relatively well after adjusting for inland water and wetland abrupt thaw flux (Table 4). The two bottom-up approaches also consistently point to a CO_2 sink in the boreal zone, but CO_2 source from the tundra (Table 3; Figures S3 and S4 in Supporting Information S1; Ramage et al., 2024). The bottom-up tundra budgets can be compared to a previous RECCAP synthesis for Arctic tundra (McGuire et al., 2012) reporting a Tundra biome CO_2 sink and CH_4 source from both data-driven and process models over 1990–2006 (−103 and −177 Tg CO_2-C yr^{-1} and 11 and 26 Tg CH_4-C yr^{-1}, respectively). The discrepancy in relation to our tundra CO_2 budget (suggesting a source) is only partly explained by the inclusion of inland water CO_2 sources, since the process-based models and CARDAMOM show a near-neutral tundra CO_2 budget (Figure S3 in Supporting Information S1).

The top-down flux estimates were extracted from global inversion model systems showing a large variance between the different inversion model frameworks (Tables S4–S6 in Supporting Information S1). This large variance may partly be explained by a relatively limited set of atmospheric concentration observations available for the region, both from the surface networks or satellite observing systems. For instance, recent work showed that the majority of the CH_4 sources currently present in high northern latitudes are poorly constrained by the existing observation network (Wittig et al., 2023; Yuan et al., 2024). Furthermore, the resolution at which fluxes are estimated is coarse in comparison to the large landscape heterogeneity of the studied region (e.g., Treat et al., 2008b; Treat, Bloom, & Marushchak, 2018); this might increase variability between different inversion systems and contribute to the systematic differences in relation to bottom-up approaches. A recent study using an ensemble of bottom-up and top-down approaches and the FLUXNET-CH_4 emission data set found that neither approach accurately captured the observed CH_4 emissions, and that down-selecting the best (against observed CH_4 emissions) bottom-up and top-down approaches did not reduce these discrepancies (Chang et al., 2023).

Another potential source of mismatch between bottom-up and top-down estimates is the source of information used to estimate prior fluxes for the GHG inversion systems. It is possible that if prior flux ensembles consistently included all of the land cover types and processes included in bottom-up estimates, they would be more similar. For instance, the global inversions do not include emissions from inland water as prior knowledge for the inversion system (Table S3 in Supporting Information S1 and references therein). For CO_2, the prior fluxes are based on land surface models and fire inventories as well as anthropogenic emissions, with systems optimized to estimate fluxes from the natural ecosystems (Friedlingstein et al., 2022). For CH_4, the prior fluxes included only emissions estimated from process-based models for wetlands and anthropogenic sources (Saunois et al., 2020). Inland waters

are important sources of all GHGs, with a combined emission of 333 (181, 501) Tg CO_2-Ceq yr^{-1} (Table 7). Adding inland water emissions to the prior flux ensemble may help reconcile bottom-up and top-down estimates. We note that the budgets estimated by the inversion ensembles are relatively similar to the budgets estimated by process-based models which have been used as priors. The NEE as well as wetland CH_4 fluxes derived from process-model ensembles are similar to the atmospheric inverse model CO_2 and CH_4 budgets, respectively (−450 and −587 Tg CO_2-C yr^{-1} as well as 12 and 15 Tg CH_4-C yr^{-1}, respectively). It is possible that in regions with limited atmospheric observations, the posterior fluxes do not deviate much from the priors. This problem may be particularly important during the long cold season. Shoulder-seasons and winter fluxes of both CO_2 and CH_4 are significant parts of the annual budgets in field measurements across multiple sites, but process-based models (used as inversion priors) capture these emissions poorly (Natali et al., 2019; Treat, Marushchak, et al., 2018). This bias may be further exacerbated by the systematic lack of observational constraints during winter. The observational networks for GHG fluxes in the permafrost region during winter are very sparse, especially in Canada and Russia (Pallandt et al., 2022). Furthermore, the inverse model systems that use satellite instruments need enough insolation to measure the CO_2 or CH_4 atmospheric columns, limiting high-latitude winter acquisitions.

But even with updated prior fluxes, it is probable that estimates from bottom-up approaches would still be higher than the atmospheric constraint. This suggests a need for further revising the bottom-up upscaling methods in parallel with the development of top-down methods and data sets. The spatial products used to delineate the surface area of land cover types for this study remain coarse (Olefeldt et al., 2021) both in terms of spatial resolution and the diversity of land form classes (Ramage et al., 2024). Coming generations of remote sensing products are likely to improve estimates of areas of different important land cover classes. In addition to uncertain areal coverage of key land cover classes, the bottom-up budgets for all GHGs are strongly affected by average fluxes from individual land cover classes. Because of the heterogeneous nature of GHG fluxes in both space and time, it is challenging to generate data sets with unbiased and accurate annual GHG budgets (Rößger et al., 2019; Treat, Bloom, & Marushchak, 2018). There is a risk of bias toward measurements of high fluxes associated with spatial and temporal variability both within and across land cover types. There is also a risk for higher reporting prevalence from sites with high emissions, or that land cover types that are weak sinks of GHGs (but may cover large areas) are under-reported. For example, spatially widespread but weak soil CH_4 sinks are important for full tundra landscape budgets (Juncher Jørgensen et al., 2015; Juutinen et al., 2022). Larger regional gaps in observational flux networks may also be important (López-Blanco et al., 2024; Pallandt et al., 2022; Virkkala et al., 2018), because different regions can have highly diverse environmental conditions and rates of warming, shifts in biodiversity, and permafrost thaw, which can impact GHG fluxes. For example, the CO_2 balance differs between tundra and boreal regions within the permafrost zone (Treat et al., 2024). The formation and past history of permafrost deposits in different regions also influence the potential permafrost GHG feedback strengths (Jones et al., 2023), which may bias estimates if field data are unevenly spaced.

Finally, there is a need for better representation of disturbance regimes, particularly as permafrost landscapes are becoming ever less static (Treat et al., 2024). This includes both fluxes from disturbance events as well as post-disturbance trajectories. Sinks of CO_2 have been observed during post-fire recovery (Walker et al., 2019) or after insect outbreaks (Lund et al., 2017). However, other studies suggest more uncertain post-disturbance trajectories of all three GHGs, including sustained CO_2 sources, CH_4 sinks and limited impact on N_2O fluxes (Hermesdorf et al., 2022; Köster et al., 2017; Schulze et al., 2023). Another large source of uncertainty is how abrupt permafrost thaw affects GHG budgets. In our budgets, abrupt thaw is entirely missing in the process models but partly included in the data-driven upscaling and integrated bottom-up budgets. The spatial extent and annual fluxes of abrupt thaw landforms remain poorly constrained (Turetsky et al., 2020). In addition, abrupt thaw landforms and other disturbed soils may emit N_2O (Voigt et al., 2020), but this is not included in any of our budgeting approaches due to the lack of in situ observations. Further improvements to data-driven bottom-up budgets could be made by (a) an increased number of observations, including more spatially unbiased and more distributed data and non-growing season measurements, (b) consistent reporting of net-zero or negative fluxes to prevent biased site selection and reporting in published literature and (c) upscaling using techniques that can simultaneously consider several environmental conditions and their variability across the entire permafrost region (Natali et al., 2019; Virkkala et al., 2021).

4. Conclusions

We present the first synthesis of GHG budgets for CO_2, CH_4 and N_2O as well as lateral fluxes of C and N across the northern terrestrial permafrost region using bottom-up (ecosystem flux upscaling and process-based models) and top-down (atmospheric inversion models) approaches for the period 2000–2020. Bottom-up approaches consistently yield estimates of stronger GHG sources compared to top- down approaches. Both approaches show a net sink of CO_2 in natural ecosystems, but they diverge by several hundred Tg CO_2-C yr^{-1} (bottom-up: −29 (−709, 455), top-down: −587 (−862, −312)). The Boreal biome, especially the Boreal forest land cover, is a stronger net sink, while the Tundra biome is neutral, or even a source when accounting for fluxes from inland waters. Bottom-up and top-down approaches both show sources of CH_4 but the 95% CI ranges do not overlap (bottom-up: 38 (22, 53), top-down: 15 (11, 18) Tg CH_4-C yr^{-1}). The strongest sources of CH_4 are permafrost-free wetlands, and inland waters. Estimates of N_2O are highly uncertain, but both methods estimate sources to the atmosphere (bottom-up: 0.7 (0.07, 1.3), top-down: 0.09 (−0.19, 0.37) Tg N_2O-N yr^{-1}). Anthropogenic emissions from the region are 73 (56, 89) Tg CO_2-C yr^{-1} and 5.4 (3.8, 7.1) Tg CH_4-C yr^{-1}, in both cases dominated by combustion of fossil fuels (estimates not available for N_2O). The century-scale global warming potential (GWP-100) ranges from a bottom-up source of 597 (−355, 1,342) to a top-down sink of −285 (−668, 86) Tg CO_2-C_{eq} yr^{-1}. Over shorter timescales (GWP-20), both approaches show a net source of global warming potential (bottom-up: 1394 (129, 2427), top-down: 81 (−399, 533) Tg CO_2-C_{eq} yr^{-1}). Estimated total C stock change budgets diverge from source to sink (bottom-up: 107 (−556, 729), top-down: −479 (−772, −183)), but converge on a N stock change source (bottom-up: 3.3 (2.0, 4.9), top-down: 2.7 (1.7, 4.0)).

Inverse model data sets have not been extensively used for studies of the permafrost region, but are highly useful for large-scale budgets and should be utilized to a greater degree in future studies. The consistently higher bottom-up land-to-atmosphere fluxes compared to top-down inversions points to potential systematic biases in both or either of these methods. Future efforts should focus on improved observational networks to support atmospheric inversions in the region and comparison of spatial patterns within atmospheric inversion models, including analysis of how prior fluxes affect the posterior budgets. Data-driven bottom-up estimates are still data-limited and further refinement of the spatial resolution and GHG balances for individual classes could improve estimates. Process-based model estimates are highly useful and complementary to other budgeting approaches. With future addition or improvement of key processes, such as abrupt thaw and inland water dynamics, it is likely that budgets from process-based models would be similar to data-driven upscaling. If it can be shown that process-based models mimic data-constrained estimates for present day budgets, it increases confidence in using models for projections of future GHG dynamics.

In summary, the permafrost region budgets suggest a weak CO_2 sink and stable sources of CH_4 and N_2O, but magnitudes differ between top-down and bottom-up methods. Although some consistent patterns emerge, we cannot fully reconcile bottom-up and top-down GHG budgets for the permafrost region. The bottom-up budget may be systematically biased in ways that increase estimated fluxes to the atmosphere from high-emitting land cover types, while top-down atmospheric inversion budgets may be systematically biased in ways that decrease fluxes to the atmosphere by not including ecosystem types that are known net GHG sources in prior flux estimates. Considering these systematic constraints in both methods, it is likely that improved estimates would yield budgets that fall between the two separate estimates presented here for all three GHGs. We can conclude that the northern permafrost region is a net source of combined global warming potential over decadal time-scales (GWP-20). The total C budget and century-scale global warming potential (GWP-100) have large uncertainties and are indistinguishable from neutral. The Boreal biome is likely a C sink, and near neutral for GHGs. The Tundra biome is likely near neutral for C stock change but a GHG source.

Data Availability Statement

Process-based model simulations were accessed from their archives, including the CMIP5 archive (https://esgf-node.llnl.gov/search/cmip5) and CMIP6 archive (https://esgf-node.llnl.gov/search/cmip6). We downloaded and extracted carbon stocks and fluxes from both the Permafrost Carbon Network (PCN) and Multi-scale Synthesis and Terrestrial Model Intercomparison Project (MsTMIP) ensembles via the ORNL DAAC (Huntzinger et al., 2018; McGuire et al., 2022, respectively). Data from the Inter-Sectoral Impact Model Intercomparison Project phases 2 and 3 (ISIMIP2a and ISIMIP2b) is available from https://www.isimip.org. CARDAMOM data is

Acknowledgments
This work is a collaborative effort from the Global Carbon Project Second REgional Carbon Cycle and Processes study (RECCAP2) and contributes to the Arctic Methane and Permafrost Challenge (AMPAC). JR and GH acknowledge support from the European Union's Horizon 2020 Research and Innovation Programme to the Nunataryuk project (773421) and support from the AMPAC-Net project funded by the European Space Agency (ESA). GH acknowledges the Swedish Research Council VR (Grant 2022-04839). JR received additional funding from the Swedish Academy of Science (Formas) under the Grant FR-2021/0004. EJB has received funding from the European Union's Horizon 2020 research and innovation programme under Grant Agreement No 101003536 (ESM2025–Earth System models for the Future) and from the Joint UK BEIS/Defra Met Office Hadley Centre Climate Programme (GA01101). The work of AC and JL was conducted at the Jet Propulsion Laboratory, California Institute of Technology, under a contract with the National Aeronautics and Space Administration (80NM0018D0004), and AC was supported by NASA Grant/Cooperative Agreement Number: NNX17AD69A. Work of MEM was supported by the Academy of Finland in the frame of the Atmosphere and Climate Competence Center (ACCC) (337550). CV was supported by the Academy of Finland project MUFFIN (Grant 332196) and the project MOMENT (03F0931A) funded by the German Federal Ministry of Education and Research (BMBF). CB wishes to thank the Academy of Finland (project N-PERM–decision no 341348, project NOCA–decision no. 314630 and the Yedoma-N project decision no. 287469)) for financial support, as well as the PERNO project supported by FWF, Austria (Grant M03335). AMV, BMR, SMN, JDW, and SP were funded by the Gordon and Betty Moore foundation (Grant 8414) and through funding catalyzed by the Audacious Project (Permafrost Pathways). MAK was supported by the NSF PRFB Program (Abstract # 2109429). TK acknowledges support through the project Palmod, funded by the German Federal Ministry of Education and Research (BMBF), Grant 01LP1921A. JGC was funded by the Australian National Environmental Science Program (NESP2)–Climate Systems Hub. MIROC4-ACTM inversion activity is supported by the Arctic Challenge for Sustainability phase II (ArCS-II; JPMXD1420318865) Projects of the Ministry of Education, Culture, Sports, Science and Technology (MEXT), and Environment Research and Technology Development Fund (JPMEERF21S20800) of the Environmental Restoration and Conservation Agency of Japan. TLS, PIP

available via https://doi.org/10.7488/ds/7505. All data sources for data-driven ecosystem upscaling are provided by Ramage et al. (2024). Monthly data for all models included in the top-down inversion ensembles are available via the Bolin Centre Database (Hugelius et al., 2024). The CARDAMOM-permafrost data set can be freely downloaded from https://doi.org/10.7488/ds/7505.

References

Aas, K. S., Martin, L., Nitzbon, J., Langer, M., Boike, J., Lee, H., et al. (2019). Thaw processes in ice-rich permafrost landscapes represented with laterally coupled tiles in a land surface model. *The Cryosphere*, *13*(2), 591–609. https://doi.org/10.5194/tc-13-591-2019

Abbott, B. W., Jones, J. B., Schuur, E. A. G., Chapin III, F. S., Bowden, W. B., Bret-Harte, M. S., et al. (2016). Biomass offsets little or none of permafrost carbon release from soils, streams, and wildfire: An expert assessment. *Environmental Research Letters*, *11*(3), 034014. https://doi.org/10.1088/1748-9326/11/3/034014

Andrew, R. M., & Peters, G. P. (2022). The Global Carbon Project's fossil CO_2 emissions dataset (2022v27) [Dataset]. *Zenodo*. https://doi.org/10.5281/zenodo.7215364

Biskaborn, B. K., Smith, S. L., Noetzli, J., Matthes, H., Vieira, G., Streletskiy, D. A., et al. (2019). Permafrost is warming at a global scale. *Nature Communications*, *10*(1), 264. https://doi.org/10.1038/s41467-018-08240-4

Bloom, A. A., Exbrayat, J.-F., Van Der Velde, I. R., Feng, L., & Williams, M. (2016). The decadal state of the terrestrial carbon cycle: Global retrievals of terrestrial carbon allocation, pools, and residence times. *Proceedings of the National Academy of Sciences*, *113*(5), 1285–1290. https://doi.org/10.1073/pnas.1515160113

Bloom, A. A., & Williams, M. (2015). Constraining ecosystem carbon dynamics in a data-limited world: Integrating ecological "common sense" in a model–data fusion framework. *Biogeosciences*, *12*(5), 1299–1315. https://doi.org/10.5194/bg-12-1299-2015

Bruhwiler, L., Parmentier, F.-J. W., Crill, P., Leonard, M., & Palmer, P. I. (2021). The Arctic carbon cycle and its response to changing climate. *Current Climate Change Reports*, *7*(1), 14–34. https://doi.org/10.1007/s40641-020-00169-5

Burke, E. J., Zhang, Y., & Krinner, G. (2020). Evaluating permafrost physics in the Coupled Model Intercomparison Project 6 (CMIP6) models and their sensitivity to climate change. *The Cryosphere*, *14*(9), 3155–3174. https://doi.org/10.5194/tc-14-3155-2020

Byrne, B., Liu, J., Yi, Y., Chatterjee, A., Basu, S., Cheng, R., et al. (2022). Multi-year observations reveal a larger than expected autumn respiration signal across northeast Eurasia. *Biogeosciences*, *19*(19), 4779–4799. https://doi.org/10.5194/bg-19-4779-2022

Caen, A., Smallman, T. L., De Castro, A. A., Robertson, E., Von Randow, C., Cardoso, M., & Williams, M. (2022). Evaluating two land surface models for Brazil using a full carbon cycle benchmark with uncertainties. *Climate Resilience and Sustainability*, *1*(1), e10. https://doi.org/10.1002/cli2.10

Canadell, J. G., Monteiro, P. M. S., Costa, M. H., Cotrim da Cunha, L., Cox, P. M., Eliseev, A. V., et al. (2021). Global carbon and other biogeochemical cycles and feedbacks. In V. Masson-Delmotte, P. Zhai, A. Pirani, S. L. Connors, C. Péan, S. Berger, et al. (Eds.), *Climate change 2021: The physical science basis. Contribution of working group I to the sixth assessment report of the intergovernmental panel on climate change* (pp. 673–816). Cambridge University Press. https://doi.org/10.1017/9781009157896.007

Chandra, N., Patra, P. K., Niwa, Y., Ito, A., Iida, Y., Goto, D., et al. (2022). Estimated regional CO_2 flux and uncertainty based on an ensemble of atmospheric CO_2 inversions. *Atmospheric Chemistry and Physics*, *22*(14), 9215–9243. https://doi.org/10.5194/acp-22-9215-2022

Chang, J., Ciais, P., Gasser, T., Smith, P., Herrero, M., Havlík, P., et al. (2021). Climate warming from managed grasslands cancels the cooling effect of carbon sinks in sparsely grazed and natural grasslands. *Nature Communications*, *12*(1), 118. https://doi.org/10.1038/s41467-020-20406-7

Chang, K., Riley, W. J., Collier, N., McNicol, G., Fluet-Chouinard, E., Knox, S. H., et al. (2023). Observational constraints reduce model spread but not uncertainty in global wetland methane emission estimates. *Global Change Biology*, *29*(15), 4298–4312. https://doi.org/10.1111/gcb.16755

Ciais, P., Bastos, A., Chevallier, F., Lauerwald, R., Poulter, B., Canadell, J. G., et al. (2022). Definitions and methods to estimate regional land carbon fluxes for the second phase of the REgional Carbon Cycle Assessment and Processes Project (RECCAP-2). *Geoscientific Model Development*, *15*(3), 1289–1316. https://doi.org/10.5194/gmd-15-1289-2022

Collalti, A., & Prentice, I. C. (2019). Is NPP proportional to GPP? Waring's hypothesis 20 years on. *Tree Physiology*, *39*(8), 1473–1483. https://doi.org/10.1093/treephys/tpz034

De Vrese, P., Georgievski, G., Gonzalez Rouco, J. F., Notz, D., Stacke, T., Steinert, N. J., et al. (2023). Representation of soil hydrology in permafrost regions may explain large part of inter-model spread in simulated Arctic and subarctic climate. *The Cryosphere*, *17*(5), 2095–2118. https://doi.org/10.5194/tc-17-2095-2023

Dinerstein, E., Olson, D., Joshi, A., Vynne, C., Burgess, N. D., Wikramanayake, E., et al. (2017). An ecoregion-based approach to protecting half the terrestrial realm. *BioScience*, *67*(6), 534–545. https://doi.org/10.1093/biosci/bix014

Dirmeyer, P. A., Gao, X., Zhao, M., Guo, Z., Oki, T., & Hanasaki, N. (2006). GSWP-2: Multimodel analysis and implications for our perception of the land surface. *Bulletin of the American Meteorological Society*, *87*(10), 1381–1398. https://doi.org/10.1175/BAMS-87-10-1381

European Commission Directorate-General Joint Research Centre. (2021). Leaf Area Index 1999-2020 (raster 1 km), global, 10-daily - Version 1. Retrieved from https://globalland.vito.be/geonetwork/srv/api/records/clms_global_lai_1km_v1_10daily

Famiglietti, C. A., Smallman, T. L., Levine, P. A., Flack-Prain, S., Quetin, G. R., Meyer, V., et al. (2021). Optimal model complexity for terrestrial carbon cycle prediction. *Biogeosciences*, *18*(8), 2727–2754. https://doi.org/10.5194/bg-18-2727-2021

Forster, P., Storelvmo, T., Armour, K., Collins, W., Dufresne, J.-L., Frame, D., et al. (2021). The Earth's energy budget, climate feedbacks, and climate sensitivity. In V. Masson-Delmotte, P. Zhai, A. Pirani, S. L. Connors, C. Pean, S. Berger, et al. (Eds.), *Climate change 2021: The physical science basis. Contribution of working group I to the sixth assessment report of the intergovernmental panel on climate change* (pp. 923–1054). Cambridge University Press. https://doi.org/10.1017/9781009157896.009

Foster, A. C., Wang, J. A., Frost, G. V., Davidson, S. J., Hoy, E., Turner, K. W., et al. (2022). Disturbances in north American boreal forest and Arctic tundra: Impacts, interactions, and responses. *Environmental Research Letters*, *17*(11), 113001. https://doi.org/10.1088/1748-9326/ac98d7

Friedlingstein, P., Jones, M. W., O'Sullivan, M., Andrew, R. M., Bakker, D. C. E., Hauck, J., et al. (2022). Global carbon budget 2021. *Earth System Science Data*, *14*(4), 1917–2005. https://doi.org/10.5194/essd-14-1917-2022

Gaubert, B., Stephens, B. B., Basu, S., Chevallier, F., Deng, F., Kort, E. A., et al. (2019). Global atmospheric CO_2 inverse models converging on neutral tropical land exchange, but disagreeing on fossil fuel and atmospheric growth rate. *Biogeosciences*, *16*(1), 117–134. https://doi.org/10.5194/bg-16-117-2019

Giglio, L., Boschetti, L., Roy, D. P., Humber, M. L., & Justice, C. O. (2018). The Collection 6 MODIS burned area mapping algorithm and product. *Remote Sensing of Environment*, *217*, 72–85. https://doi.org/10.1016/j.rse.2018.08.005

and LF are supported by the UK National Centre for Earth Observation funded by the Natural Environment Research Council (NE/R016518/1 and NE/N018079/1). The CARDAMOM analyses made use of resources provided by the Edinburgh Compute and Data Facility (EDCF) (http://www.ecdf.ed.ac.uk). ELB considers this study a contribution to GreenFeedBack (Greenhouse gas fluxes and earth system feedbacks) funded by the European Union's HORIZON research and innovation program under grant agreement No 101056921. EAGS was funded by NSF PLR Arctic System Science Research Networking Activities (RNA) Permafrost Carbon Network: Synthesizing Flux Observations for Benchmarking Model Projections of Permafrost Carbon Exchange (2019–2023) Grant 1931333. RL acknowledges support by the CLAND convergence institute (16-CONV-0003) funded by the French National Research Agency (ANR). Inversion studies of YN were funded by the Environment Research and Technology Development Fund (JPMEERF21S20800) of the Environmental Restoration and Conservation Agency provided by Ministry of the Environment of Japan, and supported by the NIES and MRI supercomputer systems (NEC SX-Aurora TSUBASA and FUJITSU PRIMERGY CX2550M5). WP and IL acknowledge support for using HPC cluster Aether at the University of Bremen, financed by DFG within the scope of the Excellence Initiative. JC acknowledge support from the National Key Research and Development Program of China (2022YFF0801904). RLT acknowledges support from the Copernicus Atmosphere Monitoring Service (implemented by ECMWF on behalf of the European Commission) for the CAMS N_2O inversion and the computing resources from LSCE. WJR and QZ were supported by the Reducing Uncertainties in Biogeochemical Interactions through Synthesis and Computation (RUBISCO) Scientific Focus Area sponsored by the Office of Biological and Environmental Research, Office of Science, US Department of Energy under contract DE-AC02-05CH11231.

Guimberteau, M., Zhu, D., Maignan, F., Huang, Y., Yue, C., Dantec-Nédélec, S., et al. (2018). ORCHIDEE-MICT (v8.4.1), a land surface model for the high latitudes: Model description and validation. *Geoscientific Model Development*, *11*(1), 121–163. https://doi.org/10.5194/gmd-11-121-2018

Haario, H., Saksman, E., & Tamminen, J. (2001). An adaptive metropolis algorithm. *Bernoulli*, *7*(2), 223. https://doi.org/10.2307/3318737

Hansen, M. C., Potapov, P. V., Moore, R., Hancher, M., Turubanova, S. A., Tyukavina, A., et al. (2013). High-resolution global maps of 21st-century forest cover change. *Science*, *342*(6160), 850–853. https://doi.org/10.1126/science.1244693

Harden, J. W., Koven, C. D., Ping, C.-L., Hugelius, G., David McGuire, A., Camill, P., et al. (2012). Field information links permafrost carbon to physical vulnerabilities of thawing: C and N vulerablities of thawing. *Geophysical Research Letters*, *39*(15). https://doi.org/10.1029/2012GL051958

Hermesdorf, L., Elberling, B., D'Imperio, L., Xu, W., Lambæk, A., & Ambus, P. L. (2022). Effects of fire on CO_2, CH_4, and N_2O exchange in a well-drained Arctic heath ecosystem. *Global Change Biology*, *28*(16), 4882–4899. https://doi.org/10.1111/gcb.16222

Holloway, J. E., Lewkowicz, A. G., Douglas, T. A., Li, X., Turetsky, M. R., Baltzer, J. L., & Jin, H. (2020). Impact of wildfire on permafrost landscapes: A review of recent advances and future prospects. *Permafrost and Periglacial Processes*, *31*(3), 371–382. https://doi.org/10.1002/ppp.2048

Hugelius, G., Bockheim, J. G., Camill, P., Elberling, B., Grosse, G., Harden, J. W., et al. (2013). A new data set for estimating organic carbon storage to 3 m depth in soils of the northern circumpolar permafrost region. *Earth System Science Data*, *5*(2), 393–402. https://doi.org/10.5194/essd-5-393-2013

Hugelius, G., Loisel, J., Chadburn, S., Jackson, R. B., Jones, M., MacDonald, G., et al. (2020). Large stocks of peatland carbon and nitrogen are vulnerable to permafrost thaw. *Proceedings of the National Academy of Sciences*, *117*(34), 20438–20446. https://doi.org/10.1073/pnas.1916387117

Hugelius, G., Ramage, J., Burke, E., Chatterjee, A., Smallman, T. L., Aalto, T., et al. (2024). Monthly estimated inversion model CO2, CH4 and N2O fluxes for the northern permafrost region over the period 2000-2020. *Dataset Version 1. Bolin Centre Database, Stockholm University*. https://doi.org/10.17043/hugelius-2024-permafrost-fluxes-1

Hugelius, G., Strauss, J., Zubrzycki, S., Harden, J. W., Schuur, E. A. G., Ping, C.-L., et al. (2014). Estimated stocks of circumpolar permafrost carbon with quantified uncertainty ranges and identified data gaps. *Biogeosciences*, *11*(23), 6573–6593. https://doi.org/10.5194/bg-11-6573-2014

Hugelius, G., Tarnocai, C., Broll, G., Canadell, J. G., Kuhry, P., & Swanson, D. K. (2013). The northern circumpolar soil carbon database: Spatially distributed datasets of soil coverage and soil carbon storage in the northern permafrost regions. *Earth System Science Data*, *5*(1), 3–13. https://doi.org/10.5194/essd-5-3-2013

Huntzinger, D. N., Schwalm, C. R., Wei, Y., Cook, R. B., Michalak, A. M., Schaefer, K., et al. (2018). *NACP MsTMIP: Global 0.5-degree model outputs in standard format, version 1.0*. ORNL Distributed Active Archive Center. https://doi.org/10.3334/ORNLDAAC/1225

Janssens-Maenhout, G., Crippa, M., Guizzardi, D., Muntean, M., Schaaf, E., Dentener, F., et al. (2019). EDGAR v4.3.2 Global Atlas of the three major greenhouse gas emissions for the period 1970–2012. *Earth System Science Data*, *11*(3), 959–1002. https://doi.org/10.5194/essd-11-959-2019

Jones, M. C., Grosse, G., Treat, C., Turetsky, M., Anthony, K. W., & Brosius, L. (2023). Past permafrost dynamics can inform future permafrost carbon-climate feedbacks. *Communications Earth & Environment*, *4*(1), 272. https://doi.org/10.1038/s43247-023-00886-3

Jones, M. W., Andrew, R. M., Peters, G. P., Janssens-Maenhout, G., De-Gol, A. J., Ciais, P., et al. (2021). Gridded fossil CO2 emissions and related O2 combustion consistent with national inventories 1959–2018. *Scientific Data*, *8*(1), 2. https://doi.org/10.1038/s41597-020-00779-6

Jones, M. W., Andrew, R. M., Peters, G. P., Janssens-Maenhout, G., De-Gol, A. J., Dou, X., et al. (2022). Gridded fossil CO2 emissions and related O2 combustion consistent with national inventories (GCP-GridFEDv2022.2) [Dataset]. *Zenodo*. https://doi.org/10.5281/zenodo.7016360

Juncher Jørgensen, C., Lund Johansen, K. M., Westergaard-Nielsen, A., & Elberling, B. (2015). Net regional methane sink in High Arctic soils of northeast Greenland. *Nature Geoscience*, *8*(1), 20–23. https://doi.org/10.1038/ngeo2305

Juutinen, S., Aurela, M., Tuovinen, J.-P., Ivakhov, V., Linkosalmi, M., Räsänen, A., et al. (2022). Variation in CO_2 and CH_4 fluxes among land cover types in heterogeneous Arctic tundra in northeastern Siberia. *Biogeosciences*, *19*(13), 3151–3167. https://doi.org/10.5194/bg-19-3151-2022

Kleinen, T., Mikolajewicz, U., & Brovkin, V. (2020). Terrestrial methane emissions from the Last Glacial Maximum to the preindustrial period. *Climate of the Past*, *16*(2), 575–595. https://doi.org/10.5194/cp-16-575-2020

Koren, G. (2020). *Constraining the exchange of carbon dioxide over the Amazon: New insights from stable isotopes, remote sensing and inverse modeling*. [Internal PhD, WU, Wageningen University]. Wageningen University. https://doi.org/10.18174/524771

Köster, E., Köster, K., Berninger, F., Aaltonen, H., Zhou, X., & Pumpanen, J. (2017). Carbon dioxide, methane and nitrous oxide fluxes from a fire chronosequence in subarctic boreal forests of Canada. *Science of the Total Environment*, *601–602*, 895–905. https://doi.org/10.1016/j.scitotenv.2017.05.246

Kuhn, M. A., Varner, R. K., Bastviken, D., Crill, P., MacIntyre, S., Turetsky, M., et al. (2021). BAWLD-CH_4: A comprehensive dataset of methane fluxes from boreal and arctic ecosystems. *Earth System Science Data*, *13*(11), 5151–5189. https://doi.org/10.5194/essd-13-5151-2021

Lacroix, F., Zaehle, S., Caldararu, S., Schaller, J., Stimmler, P., Holl, D., et al. (2022). Mismatch of N release from the permafrost and vegetative uptake opens pathways of increasing nitrous oxide emissions in the high Arctic. *Global Change Biology*, *28*(20), 5973–5990. https://doi.org/10.1111/gcb.16345

Lange, S. (2019). Trend-preserving bias adjustment and statistical downscaling with ISIMIP3BASD (v1.0). *Geoscientific Model Development*, *12*(7), 3055–3070. https://doi.org/10.5194/gmd-12-3055-2019

Lantuit, H., Overduin, P. P., Couture, N., Wetterich, S., Aré, F., Atkinson, D., et al. (2012). The Arctic coastal dynamics database: A new classification scheme and statistics on Arctic permafrost coastlines. *Estuaries and Coasts*, *35*(2), 383–400. https://doi.org/10.1007/s12237-010-9362-6

Lauerwald, R., Regnier, P., Figueiredo, V., Enrich-Prast, A., Bastviken, D., Lehner, B., et al. (2019). Natural lakes are a minor global source of N_2O to the atmosphere. *Global Biogeochemical Cycles*, *33*(12), 1564–1581. https://doi.org/10.1029/2019GB006261

Liu, S., Kuhn, C., Amatulli, G., Aho, K., Butman, D. E., Allen, G. H., et al. (2022). The importance of hydrology in routing terrestrial carbon to the atmosphere via global streams and rivers. *Proceedings of the National Academy of Sciences*, *119*(11), e2106322119. https://doi.org/10.1073/pnas.2106322119

Liu, Z., Kimball, J. S., Ballantyne, A. P., Parazoo, N. C., Wang, W. J., Bastos, A., et al. (2022). Respiratory loss during late-growing season determines the net carbon dioxide sink in northern permafrost regions. *Nature Communications*, *13*(1), 5626. https://doi.org/10.1038/s41467-022-33293-x

López-Blanco, E., Exbrayat, J.-F., Lund, M., Christensen, T. R., Tamstorf, M. P., Slevin, D., et al. (2019). Evaluation of terrestrial pan-Arctic carbon cycling using a data-assimilation system. *Earth System Dynamics*, *10*(2), 233–255. https://doi.org/10.5194/esd-10-233-2019

López-Blanco, E., Langen, P. L., Williams, M., Christensen, J. H., Boberg, F., Langley, K., & Christensen, T. R. (2022). The future of tundra carbon storage in Greenland – Sensitivity to climate and plant trait changes. *Science of the Total Environment*, *846*, 157385. https://doi.org/10.1016/j.scitotenv.2022.157385

López-Blanco, E., Topp-Jørgensen, E., Christensen, T. R., Rasch, M., Skov, H., Arndal, M. F., et al. (2024). Towards an increasingly biased view on Arctic change. *Nature Climate Change*, *14*(2), 152–155. https://doi.org/10.1038/s41558-023-01903-1

Lund, M., Raundrup, K., Westergaard-Nielsen, A., López-Blanco, E., Nymand, J., & Aastrup, P. (2017). Larval outbreaks in West Greenland: Instant and subsequent effects on tundra ecosystem productivity and CO2 exchange. *Ambio*, *46*(S1), 26–38. https://doi.org/10.1007/s13280-016-0863-9

Maavara, T., Lauerwald, R., Laruelle, G. G., Akbarzadeh, Z., Bouskill, N. J., Van Cappellen, P., & Regnier, P. (2019). Nitrous oxide emissions from inland waters: Are IPCC estimates too high? *Global Change Biology*, *25*(2), 473–488. https://doi.org/10.1111/gcb.14504

Marushchak, M. E., Kerttula, J., Diáková, K., Faguet, A., Gil, J., Grosse, G., et al. (2021). Thawing Yedoma permafrost is a neglected nitrous oxide source. *Nature Communications*, *12*(1), 7107. https://doi.org/10.1038/s41467-021-27386-2

Mauritsen, T., Bader, J., Becker, T., Behrens, J., Bittner, M., Brokopf, R., et al. (2019). Developments in the MPI-M earth system model version 1.2 (MPI-ESM1.2) and its response to increasing CO_2. *Journal of Advances in Modeling Earth Systems*, *11*(4), 998–1038. https://doi.org/10.1029/2018MS001400

McGuire, A. D., Christensen, T. R., Hayes, D., Heroult, A., Euskirchen, E., Kimball, J. S., et al. (2012). An assessment of the carbon balance of Arctic tundra: Comparisons among observations, process models, and atmospheric inversions. *Biogeosciences*, *9*(8), 3185–3204. https://doi.org/10.5194/bg-9-3185-2012

McGuire, A. D., Lawrence, D. M., Koven, C., Clein, J. S., Burke, E., Chen, G., et al. (2018). Dependence of the evolution of carbon dynamics in the northern permafrost region on the trajectory of climate change. *Proceedings of the National Academy of Sciences*, *115*(15), 3882–3887. https://doi.org/10.1073/pnas.1719903115

McGuire, D. A., Lawrence, D. M., Koven, C. D., Clein, J. S., Burke, E., Chen, G. S., et al. (2022). *Projections of permafrost thaw and carbon release for RCP 4.5 and 8.5* (pp. 1901–2299). ORNL Distributed Active Archive Center. https://doi.org/10.3334/ORNLDAAC/1872

Mishra, U., Hugelius, G., Shelef, E., Yang, Y., Strauss, J., Lupachev, A., et al. (2021). Spatial heterogeneity and environmental predictors of permafrost region soil organic carbon stocks. *Science Advances*, *7*(9), eaaz5236. https://doi.org/10.1126/sciadv.aaz5236

Mörner, N.-A., & Etiope, G. (2002). Carbon degassing from the lithosphere. *Global and Planetary Change*, *33*(1–2), 185–203. https://doi.org/10.1016/S0921-8181(02)00070-X

Natali, S. M., Schuur, E. A. G., Mauritz, M., Schade, J. D., Celis, G., Crummer, K. G., et al. (2015). Permafrost thaw and soil moisture driving CO_2 and CH_4 release from upland tundra. *Journal of Geophysical Research: Biogeosciences*, *120*(3), 525–537. https://doi.org/10.1002/2014JG002872

Natali, S. M., Watts, J. D., Rogers, B. M., Potter, S., Ludwig, S. M., Selbmann, A.-K., et al. (2019). Large loss of CO_2 in winter observed across the northern permafrost region. *Nature Climate Change*, *9*(11), 852–857. https://doi.org/10.1038/s41558-019-0592-8

Nitze, I., Grosse, G., Jones, B. M., Romanovsky, V. E., & Boike, J. (2018). Remote sensing quantifies widespread abundance of permafrost region disturbances across the Arctic and Subarctic. *Nature Communications*, *9*(1), 5423. https://doi.org/10.1038/s41467-018-07663-3

Obu, J. (2021). How much of the Earth's surface is underlain by permafrost? *Journal of Geophysical Research: Earth Surface*, *126*(5), e2021JF006123. https://doi.org/10.1029/2021JF006123

Obu, J., Westermann, S., Bartsch, A., Berdnikov, N., Christiansen, H. H., Dashtseren, A., et al. (2019). Northern Hemisphere permafrost map based on TTOP modelling for 2000–2016 at 1 km^2 scale. *Earth-Science Reviews*, *193*, 299–316. https://doi.org/10.1016/j.earscirev.2019.04.023

Olefeldt, D., Hovemyr, M., Kuhn, M. A., Bastviken, D., Bohn, T. J., Connolly, J., et al. (2021). The boreal–Arctic wetland and lake dataset (BAWLD). *Earth System Science Data*, *13*(11), 5127–5149. https://doi.org/10.5194/essd-13-5127-2021

Pallandt, M. M. T. A., Kumar, J., Mauritz, M., Schuur, E. A. G., Virkkala, A.-M., Celis, G., et al. (2022). Representativeness assessment of the pan-Arctic eddy covariance site network and optimized future enhancements. *Biogeosciences*, *19*(3), 559–583. https://doi.org/10.5194/bg-19-559-2022

Palmtag, J., Obu, J., Kuhry, P., Richter, A., Siewert, M. B., Weiss, N., et al. (2022). A high spatial resolution soil carbon and nitrogen dataset for the northern permafrost region based on circumpolar land cover upscaling. *Earth System Science Data*, *14*(9), 4095–4110. https://doi.org/10.5194/essd-14-4095-2022

Pandey, S., Houweling, S., Krol, M., Aben, I., Chevallier, F., Dlugokencky, E. J., et al. (2016). Inverse modeling of GOSAT-retrieved ratios of total column CH_4 and CO_2 for 2009 and 2010. *Atmospheric Chemistry and Physics*, *16*(8), 5043–5062. https://doi.org/10.5194/acp-16-5043-2016

Peylin, P., Law, R. M., Gurney, K. R., Chevallier, F., Jacobson, A. R., Maki, T., et al. (2013). Global atmospheric carbon budget: Results from an ensemble of atmospheric CO_2 inversions (preprint). *Biogeochemistry: Greenhouse Gases*. https://doi.org/10.5194/bgd-10-5301-2013

Philip, S., Johnson, M. S., Baker, D. F., Basu, S., Tiwari, Y. K., Indira, N. K., et al. (2022). OCO-2 satellite-imposed constraints on terrestrial biospheric CO_2 fluxes over South Asia. *Journal of Geophysical Research: Atmospheres*, *127*(3), e2021JD035035. https://doi.org/10.1029/2021JD035035

Potter, S., Cooperdock, S., Veraverbeke, S., Walker, X., Mack, M. C., Goetz, S. J., et al. (2023). Burned area and carbon emissions across northwestern boreal North America from 2001–2019. *Biogeosciences*, *20*(13), 2785–2804. https://doi.org/10.5194/bg-20-2785-2023

Qiu, C., Zhu, D., Ciais, P., Guenet, B., & Peng, S. (2020). The role of northern peatlands in the global carbon cycle for the 21st century. *Global Ecology and Biogeography*, *29*(5), 956–973. https://doi.org/10.1111/geb.13081

Qiu, H., Hao, D., Zeng, Y., Zhang, X., & Chen, M. (2023). Global and northern-high-latitude net ecosystem production in the 21st century from CMIP6 experiments. *Earth System Dynamics*, *14*(1), 1–16. https://doi.org/10.5194/esd-14-1-2023

Ramage, J., Kuhn, M., Virkkala, A., Voigt, C., Marushchak, M. E., Bastos, A., et al. (2024). The net GHG balance and budget of the permafrost region (2000–2020) from ecosystem flux upscaling. *Global Biogeochemical Cycles*, *38*(4), e2023GB007953. https://doi.org/10.1029/2023GB007953

Rantanen, M., Karpechko, A. Y., Lipponen, A., Nordling, K., Hyvärinen, O., Ruosteenoja, K., et al. (2022). The Arctic has warmed nearly four times faster than the globe since 1979. *Communications Earth & Environment*, *3*(1), 168. https://doi.org/10.1038/s43247-022-00498-3

Repo, M. E., Susiluoto, S., Lind, S. E., Jokinen, S., Elsakov, V., Biasi, C., et al. (2009). Large N_2O emissions from cryoturbated peat soil in tundra. *Nature Geoscience*, *2*(3), 189–192. https://doi.org/10.1038/ngeo434

Riley, W. J., Zhu, Q., & Tang, J. Y. (2018). Weaker land–climate feedbacks from nutrient uptake during photosynthesis-inactive periods. *Nature Climate Change*, *8*(11), 1002–1006. https://doi.org/10.1038/s41558-018-0325-4

Rodenhizer, H., Belshe, F., Celis, G., Ledman, J., Mauritz, M., Goetz, S., et al. (2022). Abrupt permafrost thaw accelerates carbon dioxide and methane release at a tussock tundra site. *Arctic Antarctic and Alpine Research*, *54*(1), 443–464. https://doi.org/10.1080/15230430.2022.2118639

Rousk, K., Sorensen, P. L., & Michelsen, A. (2018). What drives biological nitrogen fixation in high arctic tundra: Moisture or temperature? *Ecosphere*, *9*(2), e02117. https://doi.org/10.1002/ecs2.2117

Rößger, N., Wille, C., Veh, G., Boike, J., & Kutzbach, L. (2019). Scaling and balancing methane fluxes in a heterogeneous tundra ecosystem of the Lena River Delta. *Agricultural and Forest Meteorology*, *266–267*, 243–255. https://doi.org/10.1016/j.agrformet.2018.06.026

Runge, A., Nitze, I., & Grosse, G. (2022). Remote sensing annual dynamics of rapid permafrost thaw disturbances with LandTrendr. *Remote Sensing of Environment*, *268*, 112752. https://doi.org/10.1016/j.rse.2021.112752

Santoro, M., Cartus, O., Carvalhais, N., Rozendaal, D. M. A., Avitabile, V., Araza, A., et al. (2021). The global forest above-ground biomass pool for 2010 estimated from high-resolution satellite observations. *Earth System Science Data*, *13*(8), 3927–3950. https://doi.org/10.5194/essd-13-3927-2021

Saunois, M., Stavert, A. R., Poulter, B., Bousquet, P., Canadell, J. G., Jackson, R. B., et al. (2020). The global methane budget 2000–2017. *Earth System Science Data*, *12*(3), 1561–1623. https://doi.org/10.5194/essd-12-1561-2020

Schulze, C., Sonnentag, O., Voigt, C., Thompson, L., Van Delden, L., Heffernan, L., et al. (2023). Nitrous oxide fluxes in permafrost peatlands remain negligible after wildfire and thermokarst disturbance. *Journal of Geophysical Research: Biogeosciences*, *128*(4), e2022JG007322. https://doi.org/10.1029/2022JG007322

Schuur, E. A. G., Abbott, B. W., Commane, R., Ernakovich, J., Euskirchen, E., Hugelius, G., et al. (2022). Permafrost and climate change: Carbon cycle feedbacks from the warming Arctic. *Annual Review of Environment and Resources*, *47*(1), 343–371. https://doi.org/10.1146/annurev-environ-012220-011847

Schuur, E. A. G., Bockheim, J., Canadell, J. G., Euskirchen, E., Field, C. B., Goryachkin, S. V., et al. (2008). Vulnerability of permafrost carbon to climate change: Implications for the global carbon cycle. *BioScience*, *58*(8), 701–714. https://doi.org/10.1641/B580807

Sellar, A. A., Jones, C. G., Mulcahy, J. P., Tang, Y., Yool, A., Wiltshire, A., et al. (2019). UKESM1: Description and evaluation of the U.K. Earth system model. *Journal of Advances in Modeling Earth Systems*, *11*(12), 4513–4558. https://doi.org/10.1029/2019MS001739

Smallman, T. L., Milodowski, D. T., Neto, E. S., Koren, G., Ometto, J., & Williams, M. (2021). Parameter uncertainty dominates C cycle forecast errors over most of Brazil for the 21st Century. *Earth system interactions with the biosphere: biogeochemical cycles*. https://doi.org/10.5194/esd-2021-17

Smallman, T. L., & Williams, M. (2019). Description and validation of an intermediate complexity model for ecosystem photosynthesis and evapotranspiration: ACM-GPP-ETv1. *Geoscientific Model Development*, *12*(6), 2227–2253. https://doi.org/10.5194/gmd-12-2227-2019

Smallman, T. L., & Williams, M. (2023). Carbon and water cycle analysis across global permafrost domain, 2001–2019 [Dataset]. *University of Edinburgh. School of GeoSciences. Global Change Institute*. https://doi.org/10.7488/ds/7505

Smith, S. L., O'Neill, H. B., Isaksen, K., Noetzli, J., & Romanovsky, V. E. (2022). The changing thermal state of permafrost. *Nature Reviews Earth & Environment*, *3*(1), 10–23. https://doi.org/10.1038/s43017-021-00240-1

Stanley, E. H., Casson, N. J., Christel, S. T., Crawford, J. T., Loken, L. C., & Oliver, S. K. (2016). The ecology of methane in streams and rivers: Patterns, controls, and global significance. *Ecological Monographs*, *86*(2), 146–171. https://doi.org/10.1890/15-1027

Stell, A. C., Bertolacci, M., Zammit-Mangion, A., Rigby, M., Fraser, P. J., Harth, C. M., et al. (2022). Modelling the growth of atmospheric nitrous oxide using a global hierarchical inversion. *Atmospheric Chemistry and Physics*, *22*(19), 12945–12960. https://doi.org/10.5194/acp-22-12945-2022

Strauss, J., Abbott, B., Hugelius, G., Schuur, E. A. G., Treat, C., Fuchs, M., et al. (2021). Permafrost. In *FAO and ITPS. 2021. Recarbonizing global soils: A technical manual of recommended management practices. Volume 2: Hot spots and bright spots of soil organic carbon*. https://doi.org/10.4060/cb6378en

Tarnocai, C., Canadell, J. G., Schuur, E. A. G., Kuhry, P., Mazhitova, G., & Zimov, S. (2009). Soil organic carbon pools in the northern circumpolar permafrost region: Soil organic carbon pools. *Global Biogeochemical Cycles*, *23*(2). https://doi.org/10.1029/2008GB003327

Terhaar, J., Lauerwald, R., Regnier, P., Gruber, N., & Bopp, L. (2021). Around one third of current Arctic Ocean primary production sustained by rivers and coastal erosion. *Nature Communications*, *12*(1), 169. https://doi.org/10.1038/s41467-020-20470-z

Tian, H., Xu, R., Canadell, J. G., Thompson, R. L., Winiwarter, W., Suntharalingam, P., et al. (2020). A comprehensive quantification of global nitrous oxide sources and sinks. *Nature*, *586*(7828), 248–256. https://doi.org/10.1038/s41586-020-2780-0

Treat, C. C., Bloom, A. A., & Marushchak, M. E. (2018). Nongrowing season methane emissions-a significant component of annual emissions across northern ecosystems. *Global Change Biology*, *24*(8), 3331–3343. https://doi.org/10.1111/gcb.14137

Treat, C. C., Marushchak, M. E., Voigt, C., Zhang, Y., Tan, Z., Zhuang, Q., et al. (2018). Tundra landscape heterogeneity, not interannual variability, controls the decadal regional carbon balance in the Western Russian Arctic. *Global Change Biology*, *24*(11), 5188–5204. https://doi.org/10.1111/gcb.14421

Treat, C. C., Virkkala, A., Burke, E., Bruhwiler, L., Chatterjee, A., Fisher, J. B., et al. (2024). Permafrost carbon: Progress on understanding stocks and fluxes across northern terrestrial ecosystems. *Journal of Geophysical Research: Biogeosciences*, *129*(3), e2023JG007638. https://doi.org/10.1029/2023JG007638

Treharne, R., Rogers, B. M., Gasser, T., MacDonald, E., & Natali, S. (2022). Identifying barriers to estimating carbon release from interacting feedbacks in a warming Arctic. *Frontiers in Climate*, *3*, 716464. https://doi.org/10.3389/fclim.2021.716464

Turetsky, M. R., Abbott, B. W., Jones, M. C., Anthony, K. W., Olefeldt, D., Schuur, E. A. G., et al. (2020). Carbon release through abrupt permafrost thaw. *Nature Geoscience*, *13*(2), 138–143. https://doi.org/10.1038/s41561-019-0526-0

Van Den Hurk, B., Kim, H., Krinner, G., Seneviratne, S. I., Derksen, C., Oki, T., et al. (2016). LS3MIP (v1.0) contribution to CMIP6: The land surface, Snow and soilmoisture model intercomparison project – Aims, setup and expected outcome. *Geoscientific Model Development*, *9*(8), 2809–2832. https://doi.org/10.5194/gmd-9-2809-2016

Van Der Werf, G. R., Randerson, J. T., Giglio, L., Van Leeuwen, T. T., Chen, Y., Rogers, B. M., et al. (2017). Global fire emissions estimates during 1997–2016. *Earth System Science Data*, *9*(2), 697–720. https://doi.org/10.5194/essd-9-697-2017

Varney, R. M., Chadburn, S. E., Burke, E. J., & Cox, P. M. (2022). Evaluation of soil carbon simulation in CMIP6 Earth system models. *Biogeosciences*, *19*(19), 4671–4704. https://doi.org/10.5194/bg-19-4671-2022

Veraverbeke, S., Delcourt, C. J. F., Kukavskaya, E., Mack, M., Walker, X., Hessilt, T., et al. (2021). Direct and longer-term carbon emissions from arctic-boreal fires: A short review of recent advances. *Current Opinion in Environmental Science & Health*, *23*, 100277. https://doi.org/10.1016/j.coesh.2021.100277

Virkkala, A., Aalto, J., Rogers, B. M., Tagesson, T., Treat, C. C., Natali, S. M., et al. (2021). Statistical upscaling of ecosystem CO_2 fluxes across the terrestrial tundra and boreal domain: Regional patterns and uncertainties. *Global Change Biology*, *27*(17), 4040–4059. https://doi.org/10.1111/gcb.15659

Virkkala, A.-M., Natali, S. M., Rogers, B. M., Watts, J. D., Savage, K., Connon, S. J., et al. (2022). The ABCflux database: Arctic–boreal CO_2 flux observations and ancillary information aggregated to monthly time steps across terrestrial ecosystems. *Earth System Science Data*, *14*(1), 179–208. https://doi.org/10.5194/essd-14-179-2022

Virkkala, A.-M., Virtanen, T., Lehtonen, A., Rinne, J., & Luoto, M. (2018). The current state of CO_2 flux chamber studies in the Arctic tundra: A review. *Progress in Physical Geography: Earth and Environment*, *42*(2), 162–184. https://doi.org/10.1177/0309133317745784

Voigt, C., Lamprecht, R. E., Marushchak, M. E., Lind, S. E., Novakovskiy, A., Aurela, M., et al. (2017). Warming of subarctic tundra increases emissions of all three important greenhouse gases - Carbon dioxide, methane, and nitrous oxide. *Global Change Biology*, *23*(8), 3121–3138. https://doi.org/10.1111/gcb.13563

Voigt, C., Marushchak, M. E., Abbott, B. W., Biasi, C., Elberling, B., Siciliano, S. D., et al. (2020). Nitrous oxide emissions from permafrost-affected soils. *Nature Reviews Earth & Environment*, *1*(8), 420–434. https://doi.org/10.1038/s43017-020-0063-9

Voigt, C., Marushchak, M. E., Mastepanov, M., Lamprecht, R. E., Christensen, T. R., Dorodnikov, M., et al. (2019). Ecosystem carbon response of an Arctic peatland to simulated permafrost thaw. *Global Change Biology*, *25*(5), 1746–1764. https://doi.org/10.1111/gcb.14574

Walker, X. J., Baltzer, J. L., Cumming, S. G., Day, N. J., Ebert, C., Goetz, S., et al. (2019). Increasing wildfires threaten historic carbon sink of boreal forest soils. *Nature*, *572*(7770), 520–523. https://doi.org/10.1038/s41586-019-1474-y

Walker, X. J., Rogers, B. M., Veraverbeke, S., Johnstone, J. F., Baltzer, J. L., Barrett, K., et al. (2020). Fuel availability not fire weather controls boreal wildfire severity and carbon emissions. *Nature Climate Change*, *10*(12), 1130–1136. https://doi.org/10.1038/s41558-020-00920-8

Walter Anthony, K. M., Anthony, P., Grosse, G., & Chanton, J. (2012). Geologic methane seeps along boundaries of Arctic permafrost thaw and melting glaciers. *Nature Geoscience*, *5*(6), 419–426. https://doi.org/10.1038/ngeo1480

Wiltshire, A. J., Burke, E. J., Chadburn, S. E., Jones, C. D., Cox, P. M., Davies-Barnard, T., et al. (2021). JULES-CN: A coupled terrestrial carbon–nitrogen scheme (JULES vn5.1). *Geoscientific Model Development*, *14*(4), 2161–2186. https://doi.org/10.5194/gmd-14-2161-2021

Wittig, S., Berchet, A., Pison, I., Saunois, M., Thanwerdas, J., Martinez, A., et al. (2023). Estimating methane emissions in the Arctic nations using surface observations from 2008 to 2019. *Atmospheric Chemistry and Physics*, *23*(11), 6457–6485. https://doi.org/10.5194/acp-23-6457-2023

Yang, G., Peng, Y., Marushchak, M. E., Chen, Y., Wang, G., Li, F., et al. (2018). Magnitude and pathways of increased nitrous oxide emissions from uplands following permafrost thaw. *Environmental Science & Technology*, *52*(16), 9162–9169. https://doi.org/10.1021/acs.est.8b02271

Yu, T., & Zhuang, Q. (2020). Modeling biological nitrogen fixation in global natural terrestrial ecosystems. *Biogeosciences*, *17*(13), 3643–3657. https://doi.org/10.5194/bg-17-3643-2020

Yuan, K., Li, F., McNicol, G., Chen, M., Hoyt, A., Knox, S., et al. (2024). Boreal–Arctic wetland methane emissions modulated by warming and vegetation activity. *Nature Climate Change*, *14*(3), 282–288. https://doi.org/10.1038/s41558-024-01933-3

Yuan, Y., Zhuang, Q., Zhao, B., & Shurpali, N. (2023). Nitrous oxide emissions from pan-Arctic terrestrial ecosystems: A process-based biogeochemistry model analysis from 1969 to 2019 (preprint). *Biogeochemistry: Greenhouse Gases*. https://doi.org/10.5194/egusphere-2023-1047

Zhang, Z., Fluet-Chouinard, E., Jensen, K., McDonald, K., Hugelius, G., Gumbricht, T., et al. (2021). Development of the global dataset of wetland area and dynamics for methane modeling (WAD2M). *Earth System Science Data*, *13*(5), 2001–2023. https://doi.org/10.5194/essd-13-2001-2021

Zheng, B., Ciais, P., Chevallier, F., Yang, H., Canadell, J. G., Chen, Y., et al. (2023). Record-high CO_2 emissions from boreal fires in 2021. *Science*, *379*(6635), 912–917. https://doi.org/10.1126/science.ade0805

Zhu, Q., Riley, W. J., Tang, J., & Bouskill, N. J. (2024). Plant responses to elevated CO_2 under competing hypotheses of nitrogen and phosphorus limitations. *Ecological Applications*, *34*(3), e2967. https://doi.org/10.1002/eap.2967

Zhu, Q., Riley, W. J., Tang, J., Collier, N., Hoffman, F. M., Yang, X., & Bisht, G. (2019). Representing nitrogen, phosphorus, and carbon interactions in the E3SM land model: Development and global benchmarking. *Journal of Advances in Modeling Earth Systems*, *11*(7), 2238–2258. https://doi.org/10.1029/2018MS001571

References From the Supporting Information

Santoro, M., & Cartus, O. (2021). ESA biomass climate change initiative (Biomass_cci): Global datasets of forest above-ground biomass for the years 2010, 2017 and 2018, v2. *Centre for Environmental Data Analysis*. https://doi.org/10.5285/84403d09cef3485883158f4df2989b0c